Alma Mater Studiorum - Università di Bologna
Campus di Cesena

DIPARTIMENTO DI
INGEGNERIA DELL'ENERGIA ELETTRICA E DELL'INFORMAZIONE
"GUGLIELMO MARCONI"
Corso di Laurea Magistrale in Ingegneria Elettronica e Telecomunicazioni per l'Energia

URBAN PROPAGATION MODELING FOR NEXT-GENERATION NON-TERRESTRIAL NETWORKS

Tesi in

PROPAGAZIONE E PIANIFICAZIONE NEI SISTEMI WIRELESS LM

Relatore:
Chiar.mo Prof. Ing.
Vittorio Degli Esposti

Correlatore:
Chiar.mo Prof. Ing.
Enrico Maria Vitucci

Presentata da:
Nicolò Cenni

Anno Accademico 2022/2023

Contents

Introduction

The main purpose of the thesis project is to carry out an in-depth study of air-to-ground propagation which will secondly lead to the verification through physically consistent ray-tracing simulations in selected reference cases, of some K-factor counter-intuitive behaviours that were found by scientific community in the Third Generation Partnership Project (3GPP) Non-Terrestrial Networks (NTN) channel model. The introduction to this work aims at framing the project from a theoretical point of view by examining NTN and covering related topics such roof-to-street propagation and Rician K-factor on which much of the project analyses and considerations are based.

0.1 Non-Terrestrial Networks in next generation wireless communication systems

Non-Terrestrial Networks (NTN) are going to play a very important role in future 6th generation (6G) wireless networks, in particular research is focusing on the development of NTN in order to promote ubiquitous and high-capacity global connectivity. As stated in [1], while previous generation networks have been designed to provide connectivity for a primarily bi-dimensional space, 6G technologies involve a three-dimensional (3D) heterogeneous architecture in which terrestrial infrastructures communicate with non-terrestrial stations (different types of stations will be discussed in more detail in the next sections). The 3D structure is not only able to guarantee adequate broadband coverage to rural and unserved regions and to prevent connectivity outage during unfortunate events such as natural disasters, but can also upgrade the performance of limited terrestrial networks in a cost effective manner, ensure service availability in condition of high mobility and reinforce machine to machine communications providing service continuity.

0.1.1 Architecture

Non-terrestrial systems feature:

- A terrestrial terminal;

- An aerial/space station;
- A service link between the terrestrial terminal and the aerial/space station;
- A gateway that connects the non-terrestrial access network to the core network through a feeder link.

Figure 1 illustrates a simple satellite access network architecture.

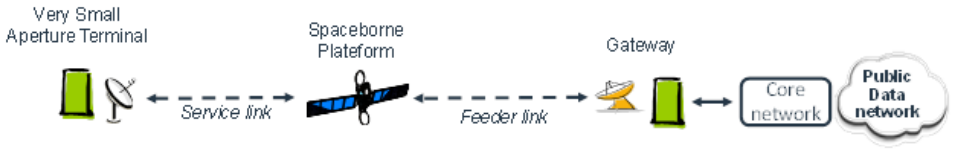

Figure 1: Example of a simple satellite access network with a service link

As explained in [1], different types of stations can be considered:

- Unmanned Aerial Vehicle (UAV): UAVs fly at low altitudes (e.g. a few hundred meters) and thanks to their flexibility, have recently gained increasing attention to provide broadband wide-scale wireless connectivity during disasters or temporary events. On the one hand, UAVs incur in high energy consumption to maintain and support their movement.
- High Altitude Platform (HAP): HAPs operate in the stratosphere at an altitude of around 20 km. They guarantee a quick deployment and a large geographic coverage.
- Satellites: Satellite stations can be classified according to their orbit characteristics. Geostationary Earth Orbit (GEO) satellites orbit on the Earth's equatorial plane at an altitude of about 35,800 km and can cover very large geographic areas. Low Earth Orbit (LEO) and Medium Earth Orbit (MEO) satellites, instead, orbit at an altitude between 200 and 2,000 km and 2,000 and 35,000 km, respectively, and guarantee better signal strength and lower propagation delay compared to GEO systems.

0.2 Roof-to-street propagation theory

In Over-Roof-Top (ORT) propagation, Roof-To-Street (RTS) propagation represents the fundamental mechanisms which allows the radio signal to reach the mobile at street level. The RTS contribution, is a complex phenomenon also involving multiple reflections and

scattering on the buildings surrounding the mobile terminal. Reflections and diffractions alone are quite inefficient for RTS propagation in dense urban environment since the former requires a large number of bounces and the latter is deep-shadow diffraction which is very weak. [2] proves how the diffuse scattering mechanism from building walls due to rough surfaces, internal irregularities and small objects is fundamental and must not be neglected when considering RTS propagation. It considers a realistic scenario built from the topology of the city of Munich (Figure 2) for which it compares simulation and measurement results showing that measurements are clearly more in agreement with the simulations that consider RTS propagation including scattering than with those that do not.

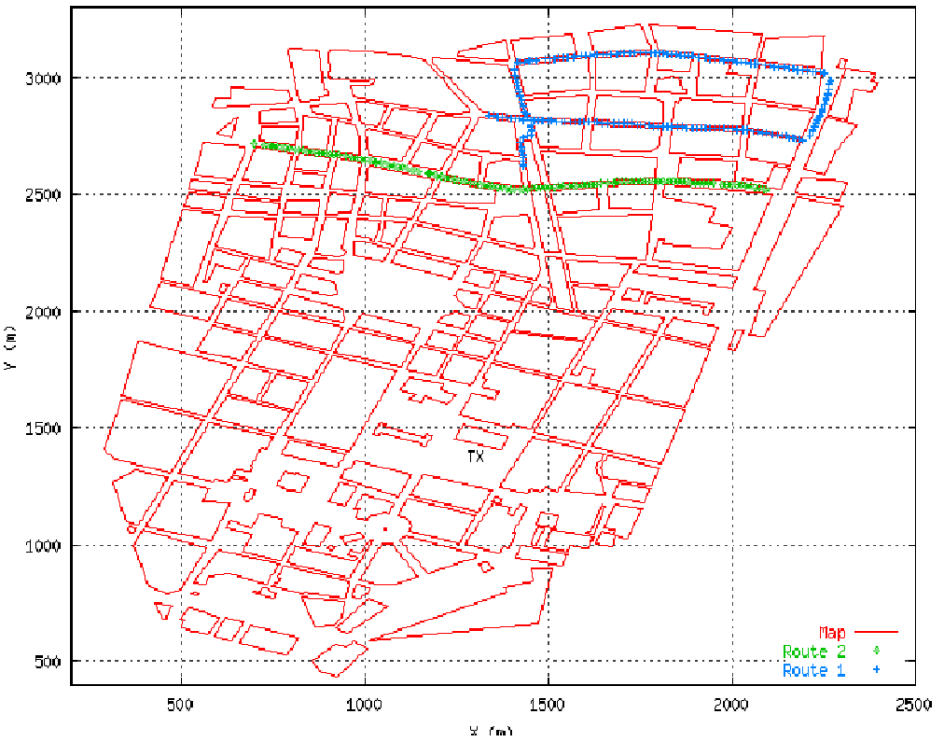

Figure 2: Topology of central Munich

0.2.1 Applications to sky-to-ground propagation and NTN

When the elevation angle of the aerial/space station is low the signal descends towards the receiver at street level via RTS propagation as shown in Figure 3. This means that at low elevation angles scattering will be dominant mechanism also in sky-to-ground propagation.

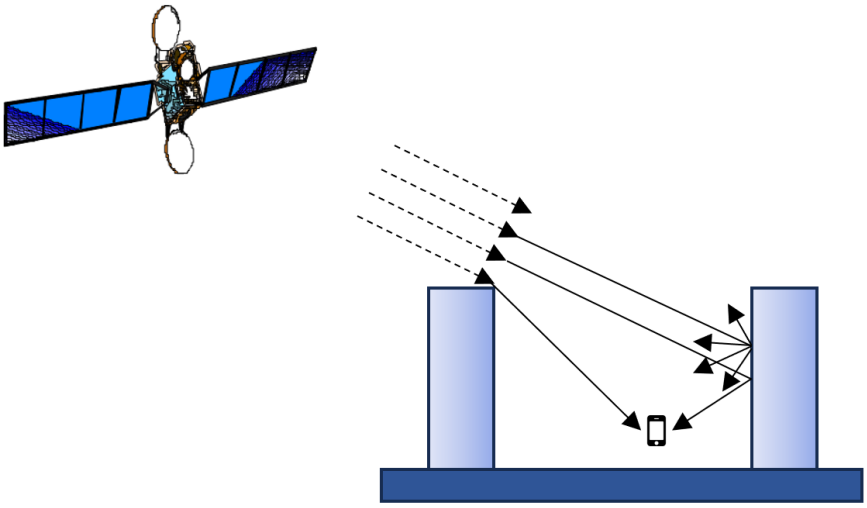

Figure 3: Roof to street propagation in air-to-ground propagation (distance not to scale)

0.3 Rician fading and K-factor

Since satellite propagation is often characterized by dominant paths, the statistic that best describes fast fading is generally Rice's. The Rician K-factor is a parameter that characterizes Rician fading in a certain propagation environment and is defined as follows.

Let X be a random variable with Rice distribution and parameters ν and σ: $X \sim \text{Rice}(\nu, \sigma)$. Then X is used to model the received signal affected by fast fading and has probability density function (pdf) that can be written as

$$f_X(x) = \frac{x}{\sigma^2} \exp\left(\frac{-(x^2+\nu^2)}{2\sigma^2}\right) I_0\left(\frac{x\,\nu}{\sigma^2}\right)$$

Where $I_0()$ is the modified Bessel function of the first kind with order zero. The K-factor (K) is defined as $K = \frac{\nu^2}{2\sigma^2}$ and it can be interpreted as the ratio between the power of the dominant component and the power of the multipath components.

Chapter 1

The 3GPP NTN channel model

The 3GPP NTN channel model is defined in [3] leveraging the 3GPP 5G channel model [4]. [3] presents different propagation parameter tables that must be used to parameterize the model according to standard scenarios (rural, suburban, urban and dense urban environments), propagation conditions (line-of-sight and non-line-of-sight), for two different frequency bands (S-band 2-4 GHz and Ka-band 27-40 GHz) i.e. the bands chosen in [3] for User Equipment and Very Small Aperture Terminal links, respectively.

1.1 Targeted user environment

Only outdoor conditions are considered for satellite operations, since performance requirements are not expected to be met with the available link budget for indoor communications. Since HAPS are closer to the Earth, resulting in less path loss than in satellite access networks, additional indoor conditions are also considered for HAPS.

1.2 Modeling objectives

The requirements for channel modelling are as follows:

- Support a frequency range from 0.5 GHz up to 100 GHz. Two frequency bands are targeted in particular: S-band and Ka-band. For Ka band communications, the uplink frequency is around 30 GHz while the downlink frequency is around 20 GHz.

- Accommodate UE mobility. For satellite channel models, mobility speed up to 1000 km/h is supported; this corresponds to aircrafts that can be served by satellite access. For HAPS channel models, mobility speed up to around 500 km/h is supported, corresponding to high speed trains.

1.3 Inconsistencies of the 3GPP NTN channel model

A look at the tables concerning the elevation dependent Rician K-factor, may raise some doubts about the validity of the model. Figure 1.1 shows some unexplained behaviours of the K-factor such as:

- Urban and rural scenarios inexplicably show a completely different trend as opposed to dense urban and suburban;
- Suburban S-band showing a higher K-factor as compared to the suburban Ka-band, while all other scenarios are showing an opposite trend;
- Almost no difference between S-band and Ka-band K-factor for the rural scenario unlike what happens in the other scenarios;
- In the urban case the K-factor decreases very rapidly as the elevation increases.

The last point is probably the most contradictory one since, given that the K-factor can be interpreted as the ratio between the power of the dominant component and the power of the other multipath components, the trend is actually expected to be the opposite. In fact, when considering an urban environment it will be precisely at higher elevations that the line of sight (LoS) will appear, dominating all the other mechanisms. Similar counter-intuitive trends can be found also in delay-spread tables.

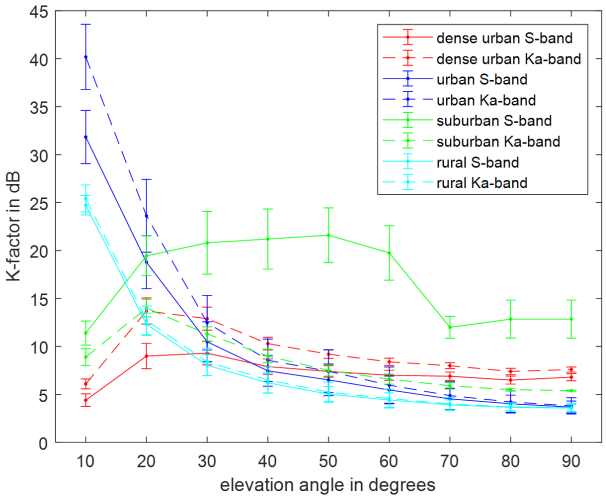

Figure 1.1: K-factor as a function of elevation angle for every scenario and frequency band, from tables in [3]

1.4 Possible cause for model inconsistencies

While there is a lot of literature discussing satellite channel models, there are not many sources considering multipath effects, as is common practice in the terrestrial channel modelling world. This lack of experimental data led to mostly relying on ray-tracing simulators to provide the required statistics needed to parameterize the 3GPP model. A very plausible cause for the inconsistencies found in the 3GPP NTN channel model is the fact that ray-tracing simulators used for the scope neglect the diffuse scattering phenomenon which is proved to be determinant in air-to-ground propagation, in particular when satellite elevation is low since both diffraction from the roof and reflection from the nearest wall turn out to be ineffective mechanisms, as described in [2] and explained in the introduction.

1.5 The Effective Roughness diffuse scattering model

The Effective Roughness model is a well-known heuristic and physically sound model that describes the electromagnetic field non-specularly reflected from a real-world surface when an incident wave is impinging on it. Its main feature is the ability to take into account phenomena that are hard to describe in a rigorous way, such as the effect of surface or internal volume irregularities, through the calibration of few parameters that allow the model to adapt to the specific situation. The basic assumption on which the model hinges on is that the incident power on a surface element is diffused according to a given scattering pattern, that consists in a lobe having maximum direction corresponding to the direction of specular reflection (Figure 1.2) while satisfying at the same time power balance and reciprocity. The latest version of the model, described in [5], is the one to be used in the ray-tracing simulations explained in the following.

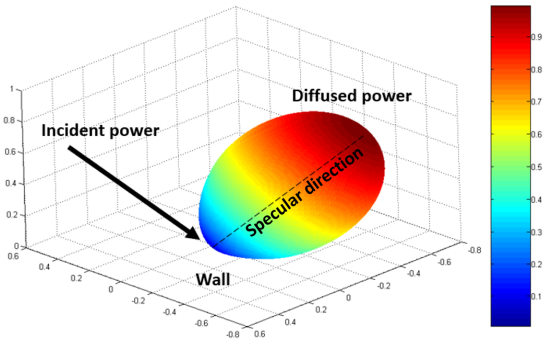

Figure 1.2: 3D scattering pattern of a surface, the incident power is diffused around the direction of specular reflection

Chapter 2

Ray-tracing simulations

The purpose of this chapter can be summarized in a few points:

- Briefly describe the choice of the simulation environment;
- Use the simulator to characterize the magnitude of the different propagation mechanisms on the overall power received, i.e. carry out an incoherent analysis that aims to study how the received power is divided between reflected rays, diffracted rays, scattered rays and rays that result from the combination of multiple mechanisms;
- Place receiver grids in significant positions of the street canyon in order to statistically characterize the small scale fading and obtain Rician K-factor tables for different elevation and azimuth angles of the transmitter.

2.1 Main features of the simulation program

The ray-tracing simulator used for this project is a sophisticated deterministic propagation prediction software based on geometric optics, its extension to diffraction (Uniform Theory of Diffraction) and diffuse scattering phenomena (Effective Roughness model). Through the simulation parameters the possibilities are almost limitless: we are able to modify the geometry and electromagnetic parameters of the building walls, position of transmitters and receivers, radiation diagram and frequency of the antennas, number of bounces of each mechanism, etc.). It is therefore an extremely complete and realistic simulator, suitable for even the most complex and realistic environments.

2.2 Ideal simulation environment

We choose to consider as simulation environment a simple Manhattan-like urban street canyon consisting of ten buildings with edges of 40 m and 30 m and streets 20 m wide

City structure	Average building height (m)	Average road width (m)
Dense urban	30	30
Urban	20	20
Suburban	10	20
Rural	5	20

Table 2.1: Geometric dimensions of buildings and streets for different types of scenarios (from [6])

(Figure 2.1). The height of the buildings is 20 m and was chosen according to Table 2.1 (from [6]). This choice of scenario is justified by the fact that, being very simple and ideal, it allows the results not to be limited solely to this environment but to provide general and valid outcomes for a large set of real urban environments.

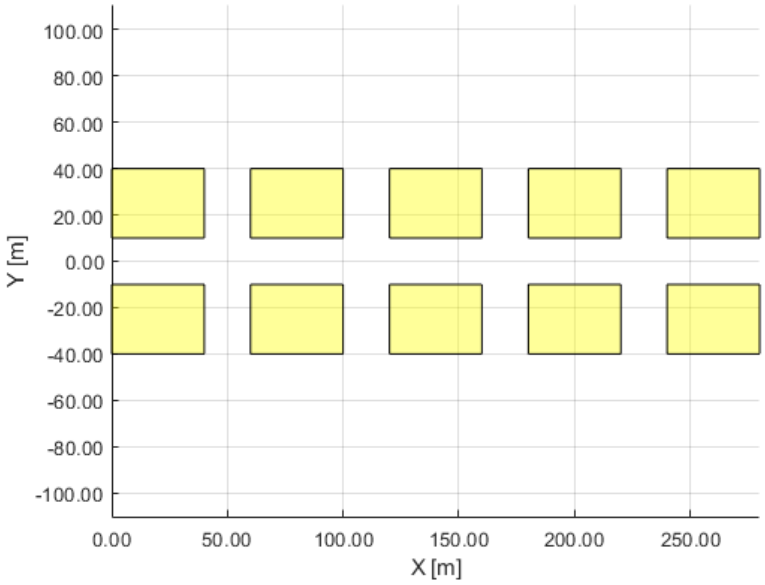

Figure 2.1: Top view of the Manhattan-like street canyon used as simulation environment in this chapter

2.2.1 Antennas

Both the transmitting and receiving antennas are assumed to be isotropic and the transmitting power is 1 dBW. As regards the frequency, it is set at 3 GHz, therefore we are considering the S-band.

2.3 Preliminary analysis of propagation mechanisms

In this section we will analyze how the overall received power is divided into the various propagation mechanisms for different receiver and transmitter positions.

2.3.1 Transmitters and receivers

We will consider only one transmitter and one receiver for each simulation. Regarding the position of the receiver, the following situations will be analyzed (refer to figure 2.2):

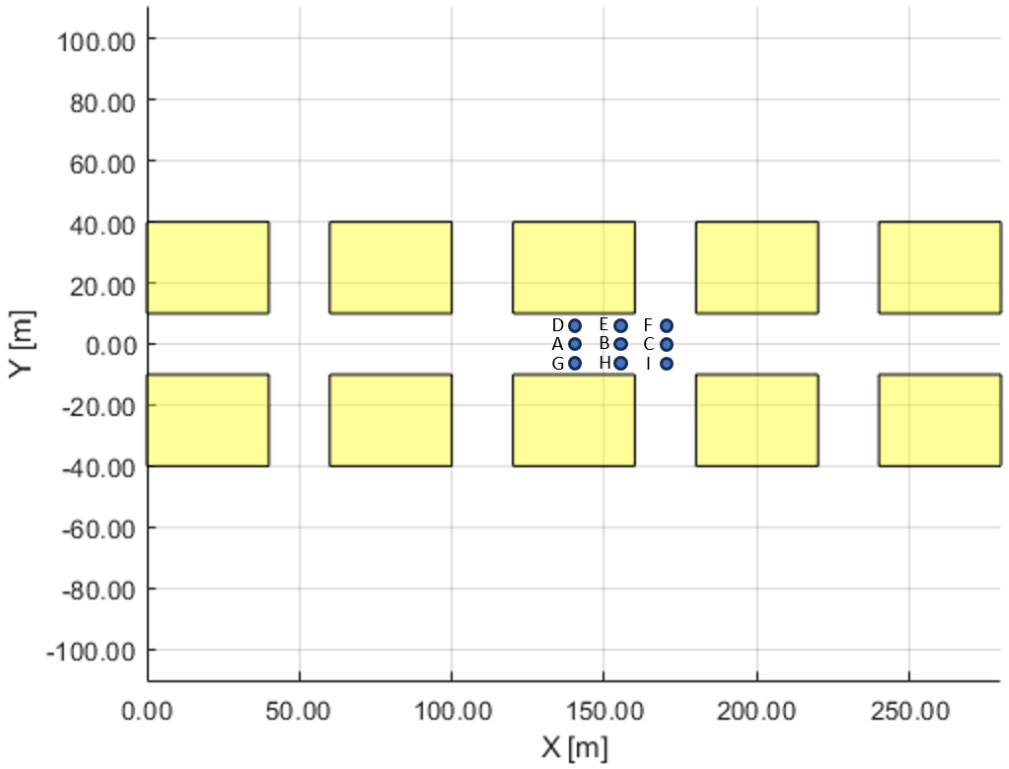

Figure 2.2: Placement of the receiver in positions A, B, C, D, E, F, G, H, I inside the street canyon

- Receiver in the middle of the street and in the center of the building (point A);
- Receiver in the middle of the street and halfway between the center of the building and the intersection (point B);
- Receiver in the middle of the street and in the center of the intersection (point C);

- Receiver near the upper building (2.5 m away from it) and in the center of the building (point D);
- Receiver near the upper building and halfway between the center of the building and the intersection (point E);
- Receiver near the upper building and in the center of the intersection (point F);
- Receiver near the lower building (2.5 m away from it) and in the center of the building (point G);
- Receiver near the lower building and halfway between the center of the building and the intersection (point H);
- Receiver near the lower building and in the center of the intersection (point I);

The receiver is located 1 m above the ground. As regards the transmitter, for each position of the receiver it will be positioned at elevations that vary between 10° and 90° (with step 10°) and azimuth between 0° and 90° (with step 45°, as shown in Figure 2.3). The distance as the crow flies between transmitter and receiver is always 281.43 m.

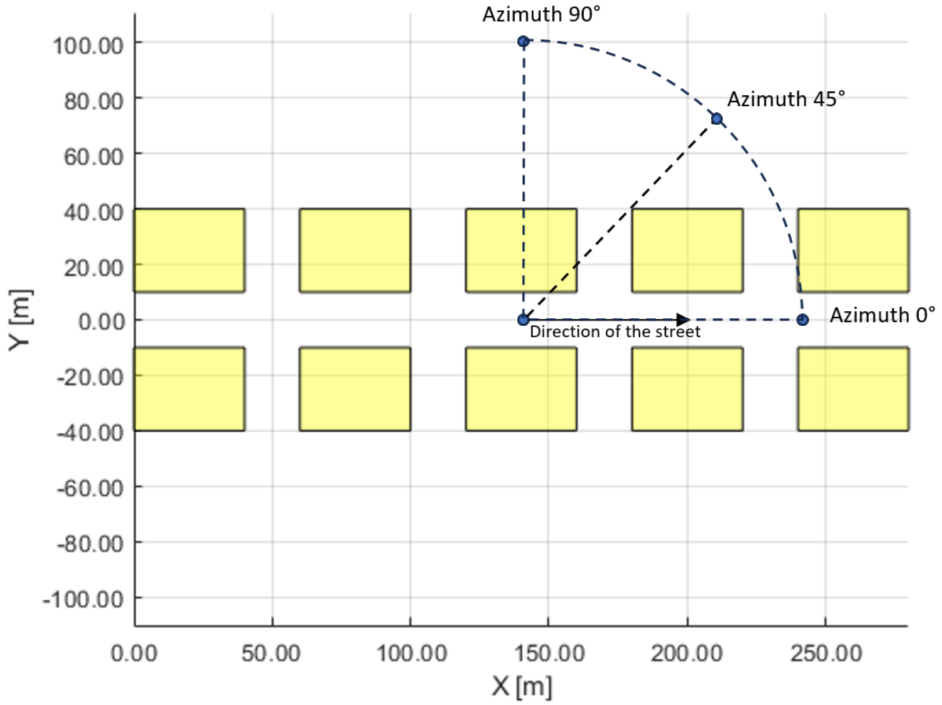

Figure 2.3: Schematic 2D representation of the reference system chosen for the azimuth angle with respect to the direction of the street, for a given position of the receiver and elevation angle

The procedure for calculating the position of the transmitter given the position of the receiver, the desired elevation and azimuth angles and the direction of the street is explained in detail in section A of the appendix. Given the symmetry of the street canyon, this choice of positions and angles ensures that the analysis of the propagation environment is, as far as possible, complete.

2.3.2 Simplified 2D analysis

Given the geometry of the scenario, factors such as the position of the receiver on the road with respect to the position of the buildings and the presence or absence of LoS have a great influence on the efficiency of the propagation mechanisms as the angles of the transmitter vary. As a reference, we discuss one particular situations in which it is possible to make interesting observations that will then be useful in the interpretation of the results of the simulations.

Let us imagine that the street canyon is composed of a single couple of buildings of infinite length in the direction of the street. Let us also imagine that the transmitter is at an azimuth angle of 90°. This hypothetical environment can be analysed, with good approximation, by studying its cross-section sketched in Figure 2.4. First of all, few parameters can be defined.

- $\theta_{2R_{MIN}}$: the minimum elevation angle necessary for the transmitter to reach the receiver via double-bounce reflection;
- $\theta_{1R_{MIN}}$: the the minimum elevation angle necessary for the transmitter to reach the receiver via single-bounce reflection from building walls;
- $\theta_{2R_{MAX}}$: the maximum elevation angle necessary for the transmitter to reach the receiver via double-bounce reflection;
- $\theta_{1R_{MAX}}$: the the maximum elevation angle necessary for the transmitter to reach the receiver via single-bounce reflection;
- $\theta_{LoS_{MIN}}$: the minimum elevation angle to have LoS.
- $\theta_{G_{MIN}}$: the the minimum elevation angle necessary for the transmitter to reach the receiver via single-bounce reflection from the ground;

Through geometric observations and applying the law of specular reflection, these parameters can be calculated for any receiver, in particular by referring to the positions of the grid in Figure 2.2, the parameters are calculated for receivers in the middle of the

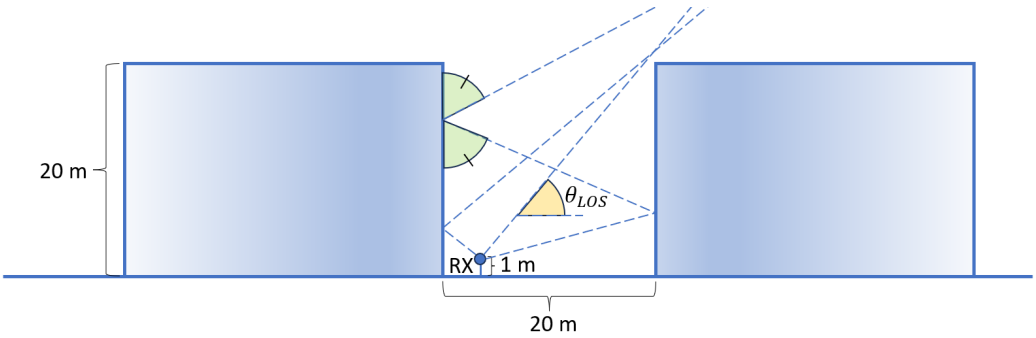

Figure 2.4: Schematic 2D representation of the cross-section of a street canyon with a single couple of buildings of infinite length in the street direction

street (point A), 2.5 m away from the upper building (point D) and 2.5 m away from the lower building (point G). The results are shown in Table 2.2.

Parameter	Point A	Point D	Point G
$\theta_{2R_{MIN}}$	23.7°	27.41°	20.84°
$\theta_{1R_{MIN}}$	34.53°	30.09°	40.84°
$\theta_{2R_{MAX}}$	36.71°	45.44°	30.55°
$\theta_{1R_{MAX}}$	65.85°	52.6°	83.51°
$\theta_{LoS_{MIN}}$	62.24°	82.5°	47.35°
$\theta_{G_{MIN}}$	64.36°	83.16°	49.93°

Table 2.2: Values of the angular parameters that allow to simplify the analysis of the mechanisms in the street canyon

Looking at Table 2.2 it is clear that the closer the receivers are to the transmitter (like in position D), the smaller the transmitter elevation angle needs to be so that a single-bounce reflection can reach them as they are further away from the building on which the reflection occurs. The opposite is true for double-bounce reflection: the closer the receivers are to the transmitter, the more the transmitter will require a higher elevation to reach them as the receivers are closer to the building on which the second reflection takes place. It is also worth noting that, given the geometry of the structure, in the same way that $\theta_{2R_{MAX}}$ is always smaller than $\theta_{1R_{MAX}}$, once the elevation angle goes past $\theta_{2R_{MAX}}$ in addition to double reflections, also triple and quadruple reflections from walls (and so on) do not exist. Furthermore, the transmitter will need a greater elevation angle to reach via LoS or ground reflection the receivers closest to it as they are hidden by the building. Obviously ground reflection can only exist for elevations higher than those necessary for LoS.

These parameters can be useful for delineating, based on the elevation angle and the position of the receiver relative to buildings, three distinct situations regarding the importance of the contribution of the individual propagation mechanisms on the overall received power as the elevation angle varies:

First of all, in all cases for small elevation angles scattering will be the predominant mechanism as already explained in the introduction. Then, as the elevation approaches and reaches $\theta_{2R_{MIN}}$ the reflection contribution will be increasingly more observable as reflections with 3 or 2 bounces will be able to reach the receiver. Then, by increasing again the elevation angle, the following situations emerge depending on the position of the receiver:

1. If the receiver is in the middle of the road (point A), the contribution of the reflections will increase more and more until we get to $\theta_{1R_{MIN}} = 34.53°$ when the reflections will become the undisputed dominant mechanism as they manage to reach the receiver through a single bounce. At elevation $\theta_{2R_{MAX}} = 36.71°$ double-bounce reflections will cease to exist, but this may not have much effect on the percentage of total received power due to reflection as the single-bounce reflections are still present. Reflections will continue to dominate until LoS appears at $\theta_{LoS_{MIN}} = 62.24°$ becoming the new dominant mechanism. At this point single bounce reflection and LoS coexist and, at elevation $\theta_G = 64.36°$, the contribution of reflection from the ground is also added. Reflection from the buildings disappears at $\theta_{1R_{MAX}} = 65.85°$ leaving room for LoS, which will remain the dominant contribution, and reflection from the ground.

2. If the receiver is located 2.5 m away from the building closer to the transmitter (point D), it is when we get to $\theta_{1R_{MIN}} = 30.09°$ that the reflections will clearly become the dominant mechanism . At elevation $\theta_{2R_{MAX}} = 45.44°$ double-bounce reflections will vanish. Reflections from the building walls will cease to exist at elevation $\theta_{1R_{MAX}} = 52.6°$ and, since LoS is not yet present, scattering and diffraction will be the remaining mechanisms. At elevation $\theta_{LoS_{MIN}} = 82.5°$ LoS appears and will remain dominant up to 90 and shortly thereafter, at $\theta_G = 83.16°$, the reflection from the ground will also be observable.

3. If the receiver is located 2.5 m away from the building furthest from the transmitter (point G) now, unlike the previous cases, double-bounce reflections will disappear before the single-bounce reflections will appear, therefore for elevations between $\theta_{2R_{MAX}} = 30.55°$ and $\theta_{1R_{MIN}} = 40.84°$ there will be no resulting power contribution from reflections. After $\theta_{1R_{MIN}}$ the single reflections will be the dominant mechanism until, at $\theta_{LoS} = 47.35°$, LoS appears and immediately afterwards, at $\theta_G = 49.93°$ also the reflection from the ground. Up to $\theta_{1R_{MAX}} = 83.51°$ the reflection contribution could be could be comparable with LoS as it is formed by both

the single bounce from buildings and from the ground, although LoS will probably still be higher. Approaching 90° LoS will increase its hegemony even more since the single-bounce reflections disappear.

Applicability

For points located far from intersections and with 90° azimuth, this simplified theory is expected to lead to accurate results also for the more complex scenario considered initially (hence for receivers A, D and G in Figure 2.2). With 45° azimuth angle reflections, diffractions and combined mechanisms could be decisive already from lower angles due to the effects of the building edges and sides. With 0° azimuth angle LoS is always present and probably dominant. Moreover, approaching the intersection the infinite street canyon approximation is no longer valid, e.g. in the extreme case in which the receiver is located at the center of the intersection and the azimuth angle is 90°, LoS is present for all the elevation angles. Scattering and diffraction contributions are difficult to predict therefore the aim of quantifying their magnitude will be left to the simulations, in any case, in the presence of LoS or single-bounce reflections, they are expected to be often almost negligible.

The results of this simulation are shown and interpreted in chapter 3, in which we also discussed how much the results reflect the theoretical analysis just performed.

2.4 Small scale fading characterization through ray-tracing simulations and post processing

In this section we wish to explain the simulations used to characterize the small scale fading in the Manhattan-like street canyon previously considered. Assuming that the variations in the received signal caused by multipath can be modeled as Rician fading we will eventually create tables that represent the K-factor as a function of the elevation angle and the azimuth angle.

2.4.1 Example of K-factor extraction

To analyze small scale fading the following approach is chosen: in order to limit the possibility of having signal variations due to shadowing, i.e. avoiding the possibility that some obstacles have repercussions on certain receivers but not on others it is best to carry out a statistical analysis of the received signal considering a set of receivers close to each other. In this first example, 300 receivers are positioned along a 1 m long segment in the middle of the road, while the transmitter is positioned at an elevation of 45° and azimuth of 90°. The variations in the received power for each receiver, obtained

by adding all the contributions in a coherent way, are shown in Figure 2.5. Thanks to the post processing explained in detail in section 2.5, knowing the received signal from each receiver, it is possible to estimate the parameters of the Rice distribution that models the small scale fading. In Figure 2.6, the Rice pdf obtained with the estimated parameters is compared with the frequency histogram of the received signal values. The estimation result is excellent, it means that the implemented procedure and the Rician model are valid for the simulation environment. Knowing the two parameters of the Rice distribution, the K-factor can be immediately calculated, in this example it is equal to 27.2 dB. Obviously the number of receivers to consider in the statistical analysis has to be be as high as possible in order to obtain a better result although the trade-off with calculation time must be taken into account.

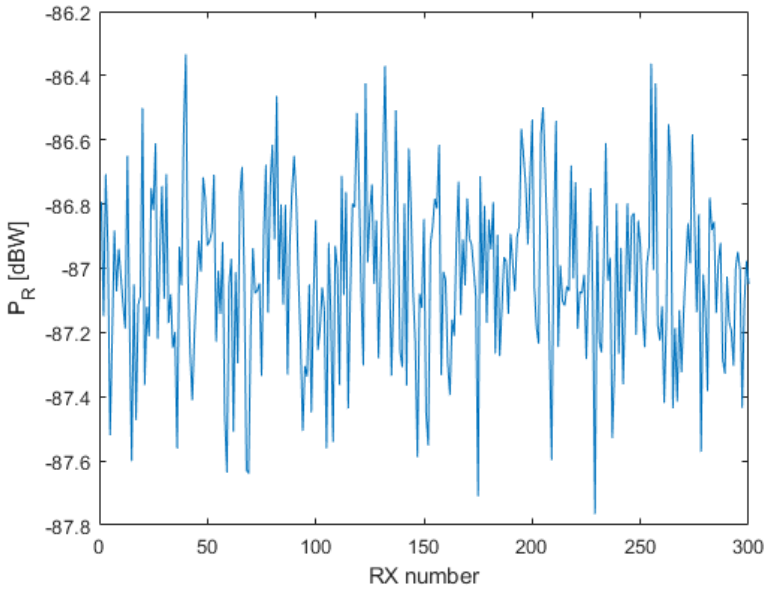

Figure 2.5: Received power for each one of the 300 receivers along a 1 m long segment in the middle of the road

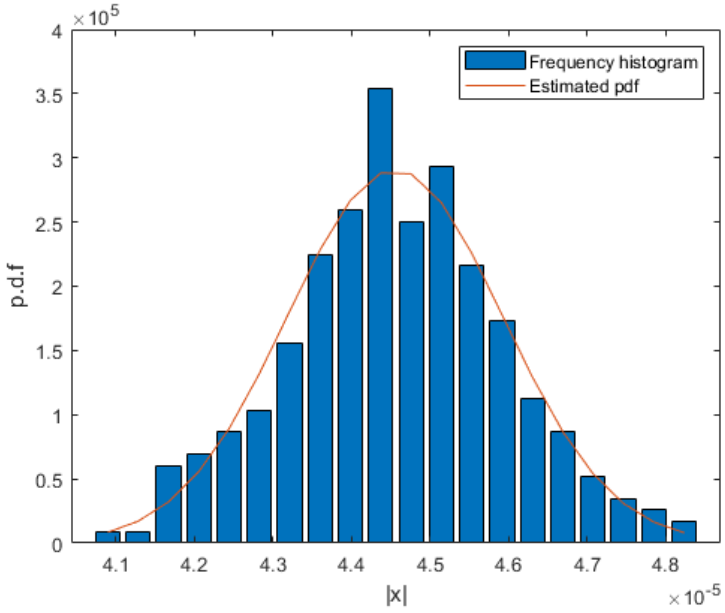

Figure 2.6: Comparison between the Rice pdf obtained with the estimated parameters and the frequency histogram of the received signal values

2.4.2 Complete environment simulation

To characterize the small scale fading over the entire propagation environment it is definitely not sufficient to calculate the K-factor at a single point for a single pair of elevation and azimuth angles. Now we choose to consider 9 square grids of 15x15 receivers with sides of 25 cm. Each of them is centered on one of the nine points A, B, D, E, F, G, H, I that were previously considered (Figure 2.7).

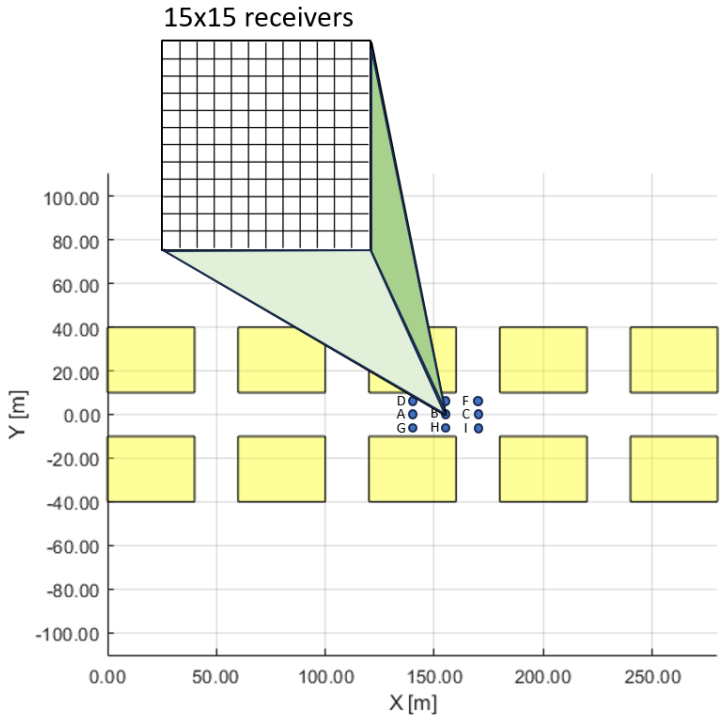

Figure 2.7: 9 grids of 15×15 receivers in positions A, B, C, D, E, F, G, H, I

Then, separately for each grid, the statistical analysis is carried out leading to the value of the K-factor for all the elevation angles between 0 and 90° with a 10° step and 90°, 45°, 0° azimuth angles (for each grid the position of the transmitter is calculated with respect to the central point). Therefore at the end of the procedure we will obtain $9 \times 9 \times 3 = 243$ values of the K-factor which will compose the desired tables.

For a fixed angle of the transmitter, it is possible to identify a sort of spatial statistics of the K-factor, which describes how it varies in the different positions of the receiver. So it will be possible, in order to make the results easier to understand, to calculate the sample mean value and standard deviation of the K-factor for each couple of elevation and azimuth angles of the transmitter.

The results of this simulation are shown and interpreted in chapter 3.

2.5 Post-processing of the simulation results

This section explains how, once the intensity of the received signal has been collected for all the receivers, it is possible to estimate the value of the K-factor.

2.5.1 Fast fading model

Let X be a random variable with Rice distribution with parameters ν and σ: $X \sim \text{Rice}(\nu, \sigma)$. X will model the intensity of the received signal.

The K-factor (K) is defined as $K = \frac{\nu^2}{2\sigma^2}$ and, as mentioned before, represents the ratio between the power of the dominant component and the power of the multipath components. Therefore to estimate the K-factor we need to estimate the parameters of the distribution using the procedure explained in the next section.

2.5.2 Maximum likelihood estimator

The problem can be formalized as follows: let us consider a certain number N of independent observations of a random variable with Rice distribution of which we want to estimate the parameters ν and σ. Let $\mathbf{x} = [x_1,\ x_2,\ \ldots,\ x_N]^T$ be the set of observations. In our case N is the number of receivers in the grid.

Opting for a maximum likelihood estimator (MLE), the result of the estimate is the pair (ν, σ) that maximize the likelyhood function, i.e.:

$$(\nu, \sigma)_{ML} = \text{argmax}_{(\nu,\theta)} \prod_{i=1}^{N} \left[\frac{x_i}{\sigma^2} \exp\left(\frac{-(x_i^2 + \nu^2)}{2\sigma^2} \right) I_0\left(\frac{x_i\,\nu}{\sigma^2} \right) \right]$$

The result is obtained numerically using MATLAB. It is worth mentioning that when the order of magnitude of the observations is very low it might be necessary to take some precautions in order to avoid warnings or errors regarding numerical difficulties during the execution of the code. For example we can normalize the N observations multiplying each one of them by a constant k so that the maximum value of $\mathbf{x}$ corresponds to 1 and, eventually, multiplying again by k both the ν and σ estimated in order not to mathematically alter the estimated distribution. This operation is mathematically justified by the property of Rice distributions explained and proved in section C of the appendix.

2.5.3 Shadowing cancellation

It is well known that small scale fading consists of oscillations of the signal observable for distances between the receivers that is often in the order of a fraction of the wavelength (λ). This is the reason why in section 2.4.2 grids of 15×15 receivers, each one spaced slightly more than ($\lambda/6$) from the next one, were used.

At the same time, shadowing causes oscillations that are visible at longer distances,

typically hundreds of λ. In case the grid cannot be made small or, despite its small dimensions, it is located in a particular position of the environment for which one or more rays reach only some of its receivers but not all of them due to obstacles, it may be useful to carry out a simple procedure on the received signal to filter out shadowing and prevent the statistical characterization of fast fading from giving wrong results. To do so we can simply carry out a moving average on the received signal, having set a certain window of W receivers. Add the overall average on all the receivers in the grid to the difference between the starting signal and its moving average and you can therefore clean up the shadowing. The moving average window W must be chosen correctly, i.e. such that the final result is cleaned of components with variations that happen for distances larger than tens/hundreds of wavelengths.

Figure 2.8 shows the frequency histogram and the estimated pdf before and after the shadowing cancellation. In the second case the statistics lends itself to being modeled according to Rice, in the first one it does not.

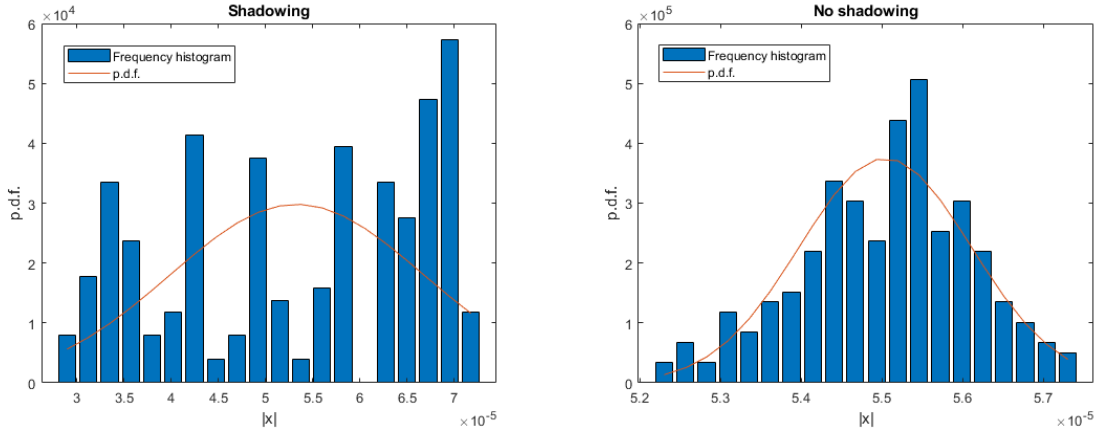

Figure 2.8: Comparison between the Rice pdf obtained with the estimated parameters and the frequency histogram of the received signal values, before and after shadowing cancellation

Chapter 3

Simulation results

3.1 Results of propagation mechanisms simulation

The results of the simulation of the environment in Figure 2.2 are shown in the following pages. For each receiver (from A to I), azimuth angle (0°, 45° and 90°) and elevation (from 10° to 90° with 10° step) a bar graph is drawn in which the percentage contributions of each mechanism on the total received power are stacked on top of each other. The propagation mechanisms that were considered in the simulation are the following:

- LoS (abbreviation L in the legend);
- Reflections, up to 4 interactions (abbreviation R);
- Diffractions, up to 3 interactions (abbreviation D);
- Reflections combined with diffractions, up to 4 interactions (abbreviation RD);
- Reflections combined with scattering, up to 2 interactions (abbreviation RS);
- Diffractions combined with scattering, 1 interaction (abbreviation DS);

We will now comment on the results one receiver at a time:

Receiver A (Figure 3.1, 3.2)

- Azimuth 90°: perfectly in agreement with the simplified 2D analysis;
- Azimuth 45°: the different angle ensures that the diffraction combined with the diffraction is observable at low elevations. Furthermore reflection is already dominant at 20° elevation, probably a new single-bounce reflected ray has appeared exploiting the lateral portion of the buildings;

- Azimuth 0°: LoS is dominant, reflection goes from 40 to 20% as elevation increases.

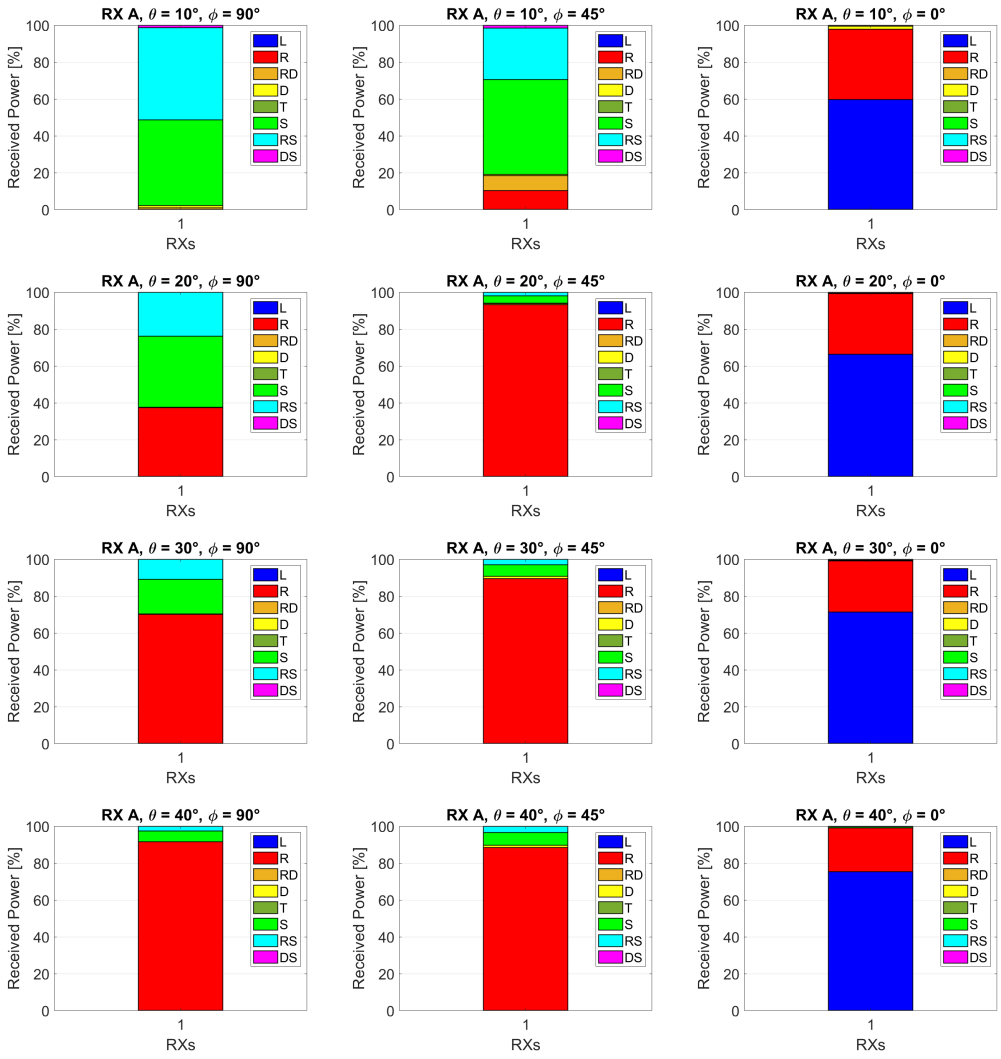

Figure 3.1: Histograms of the percentage of the total received power associated with the rays of each mechanism for the grid in position A, all azimuth angles and elevation from 10° to 40°

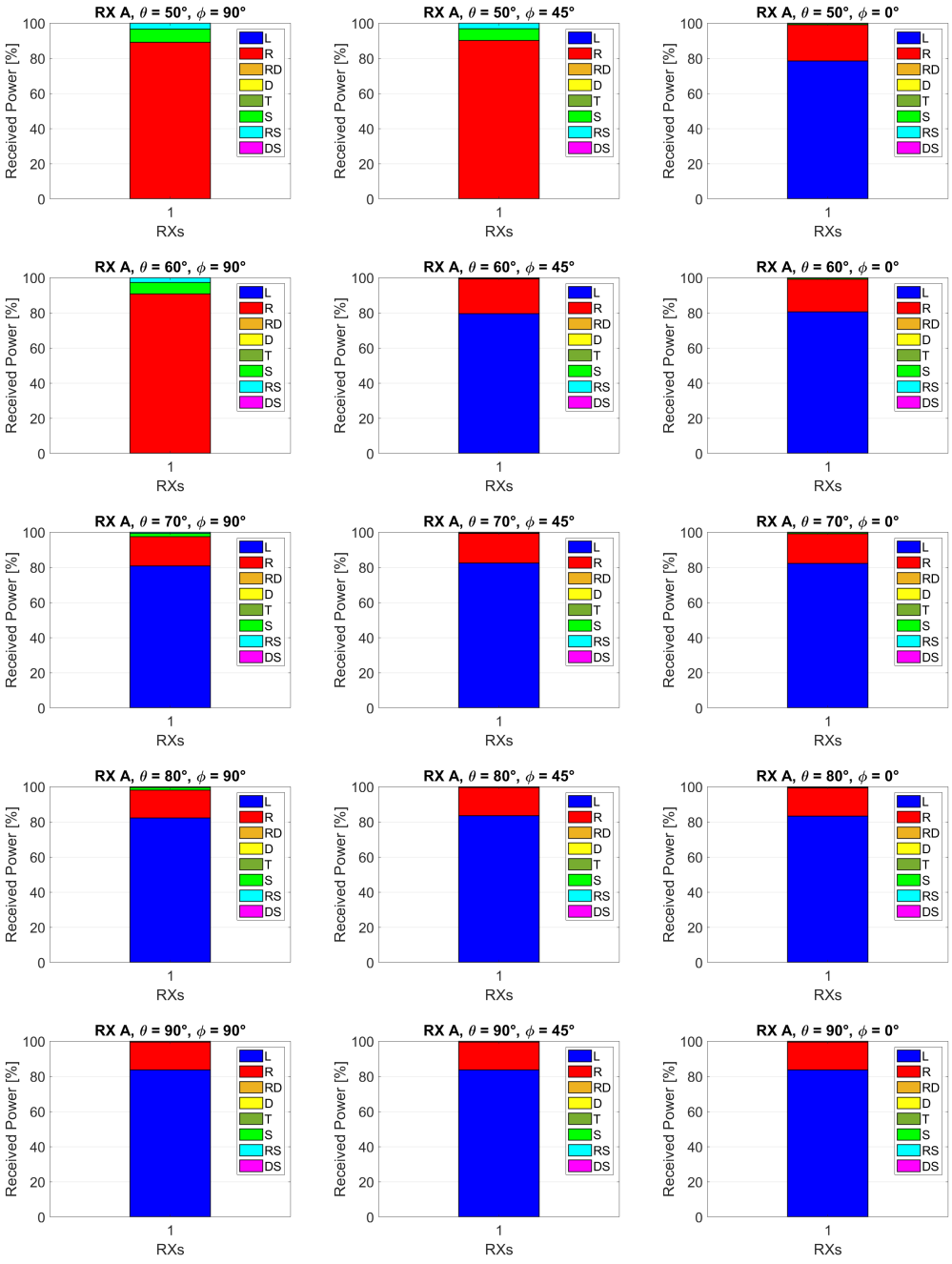

Figure 3.2: Histograms of the percentage of the total received power associated with the rays of each mechanism for the grid in position A, all azimuth angles and elevation from 50° to 90°

Receiver B (Figure 3.3, 3.4)

- Azimuth 90°: similar to A, although B is not exactly in the center of the building it follows the simplified 2D analysis;
- Azimuth 45°: at 10° and 20° of elevation reflection, scattering and diffraction are all present, with reflection having a slight edge. Suddenly reflection disappears at 30° leaving for LoS. Reflection will reappear at 30°;
- Azimuth 0°: LoS is dominant, reflection goes from 40 to 20% as elevation increases.

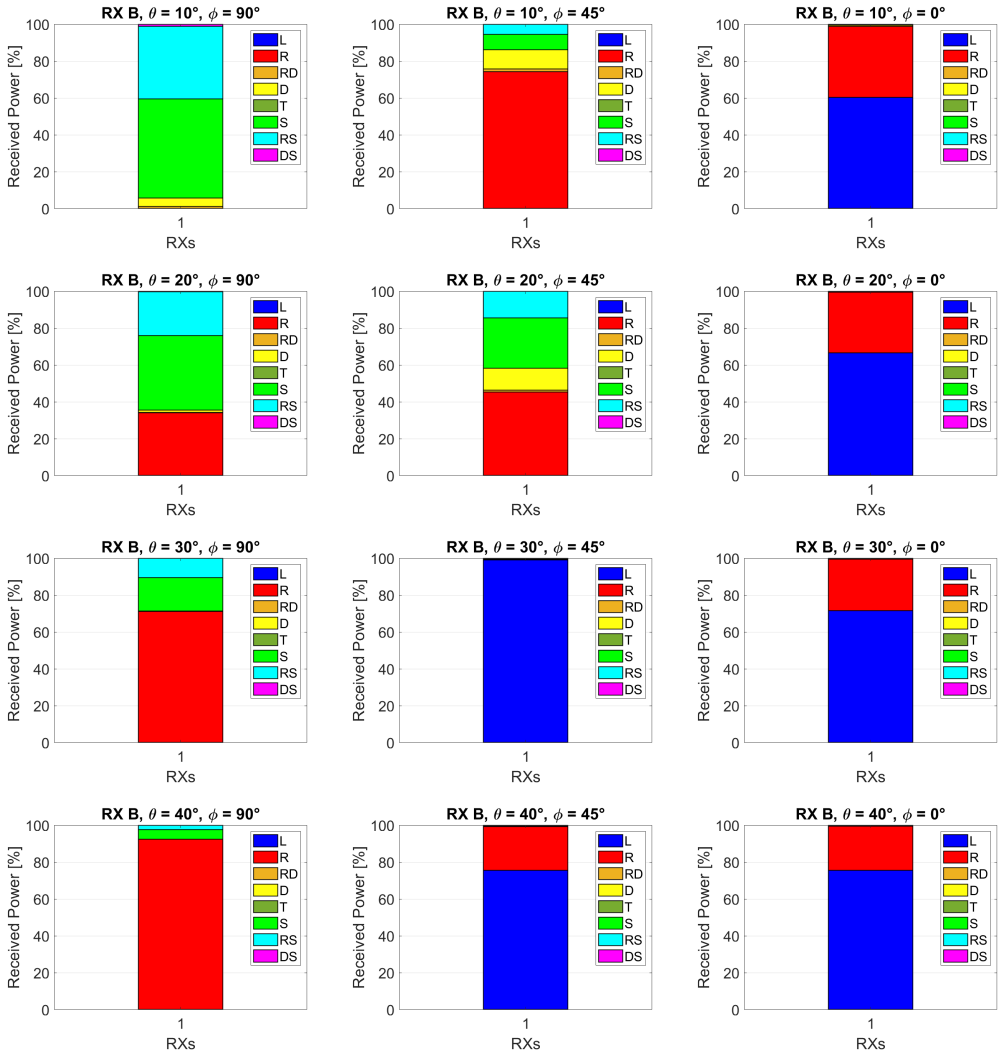

Figure 3.3: Histograms of the percentage of the total received power associated with the rays of each mechanism for the grid in position B, all azimuth angles and elevation from 10° to 40°

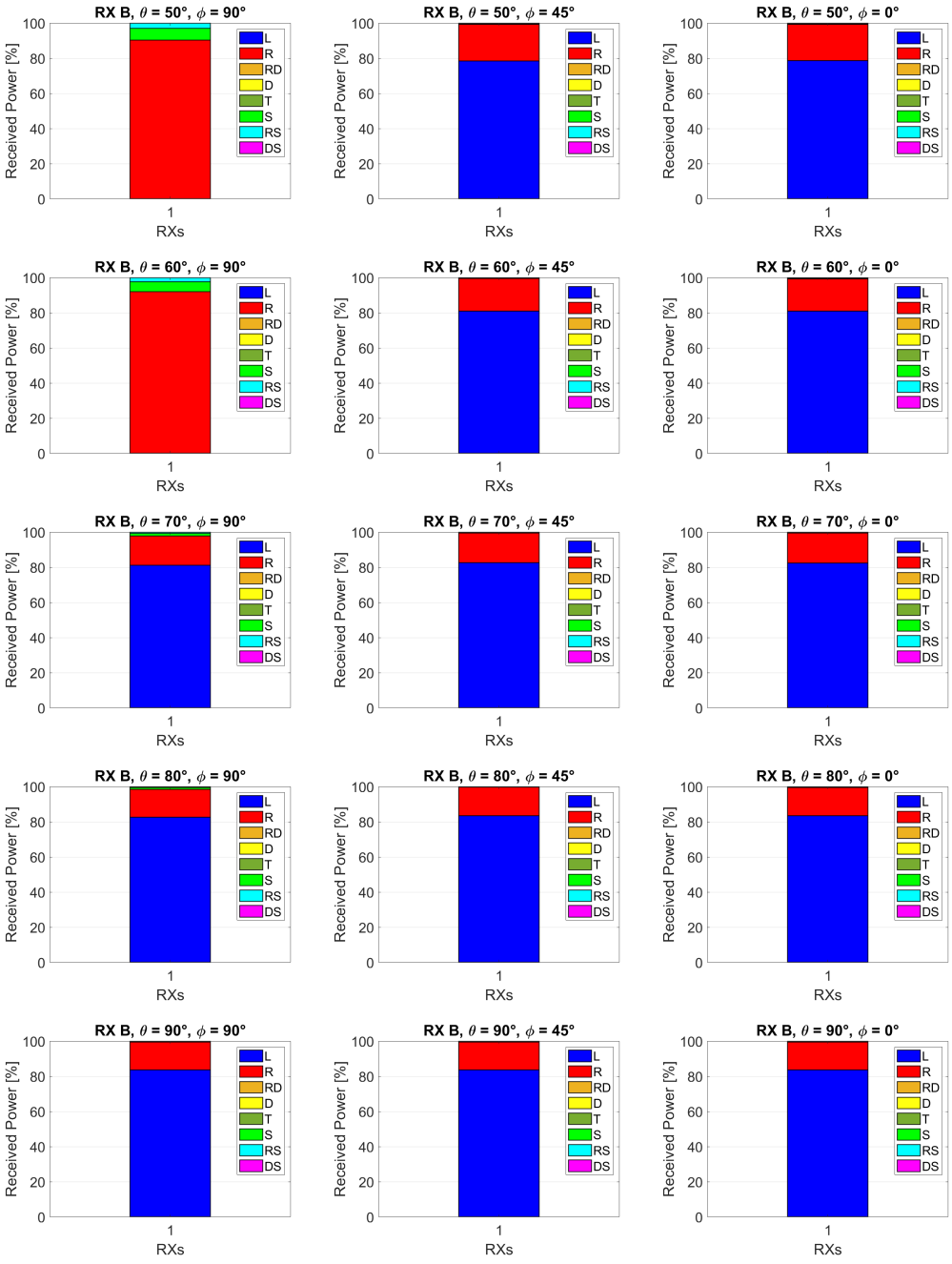

Figure 3.4: Histograms of the percentage of the total received power associated with the rays of each mechanism for the grid in position B, all azimuth angles and elevation from 50° to 90°

Receiver C (Figure 3.5, 3.6)

- Azimuth 90°: LoS is dominant, reflection goes from 40 to 20% as elevation increases;
- Azimuth 45°: up to 50° elevation scattering and diffraction take over, then only LoS and reflection remain at around 80% and 20% respectively;
- Azimuth 0°: similar to B.

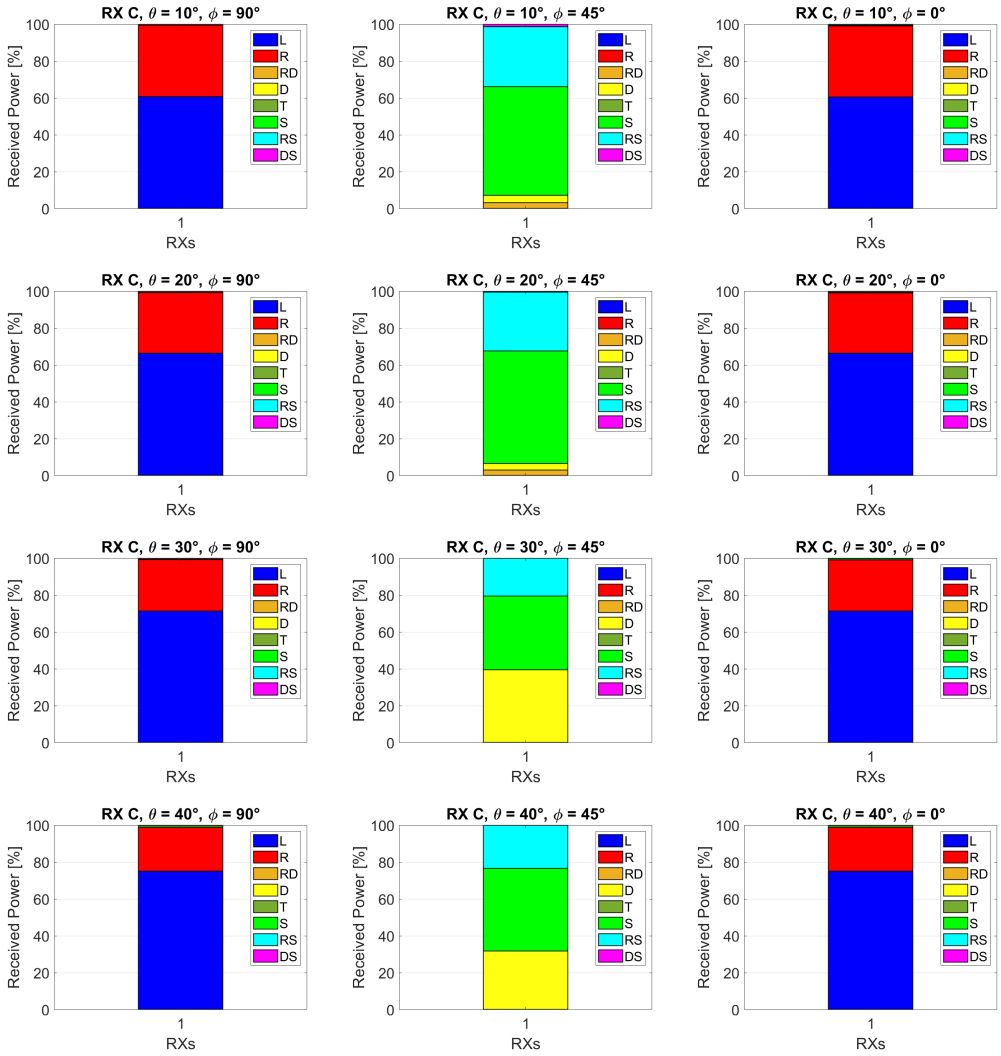

Figure 3.5: Histograms of the percentage of the total received power associated with the rays of each mechanism for the grid in position C, all azimuth angles and elevation from 10° to 40°

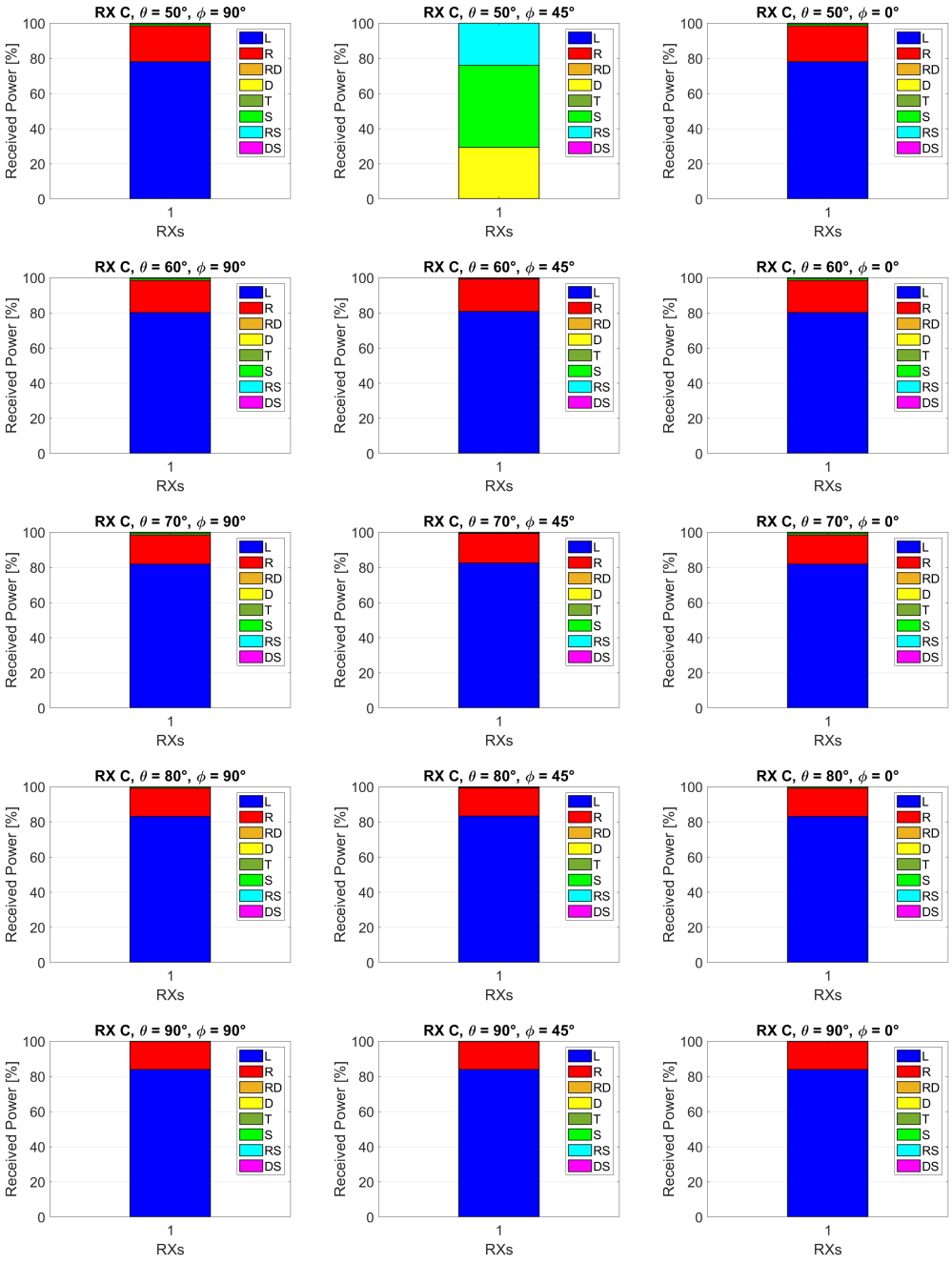

Figure 3.6: Histograms of the percentage of the total received power associated with the rays of each mechanism for the grid in position C, all azimuth angles and elevation from 50° to 90°

Receiver D (Figure 3.7, 3.8)

- Azimuth 90°: perfectly in agreement with the simplified 2D analysis;
- Azimuth 45°: reflection already appears from lower angles but disappears at 50°, where scattering dominates. At 80 there is LoS;
- Azimuth 0°: at low elevations a good portion of power comes from diffractions (roughly 15% at 10°). At higher elevations LoS is dominant, reflection goes from 40 to less than 20% as elevation increases.

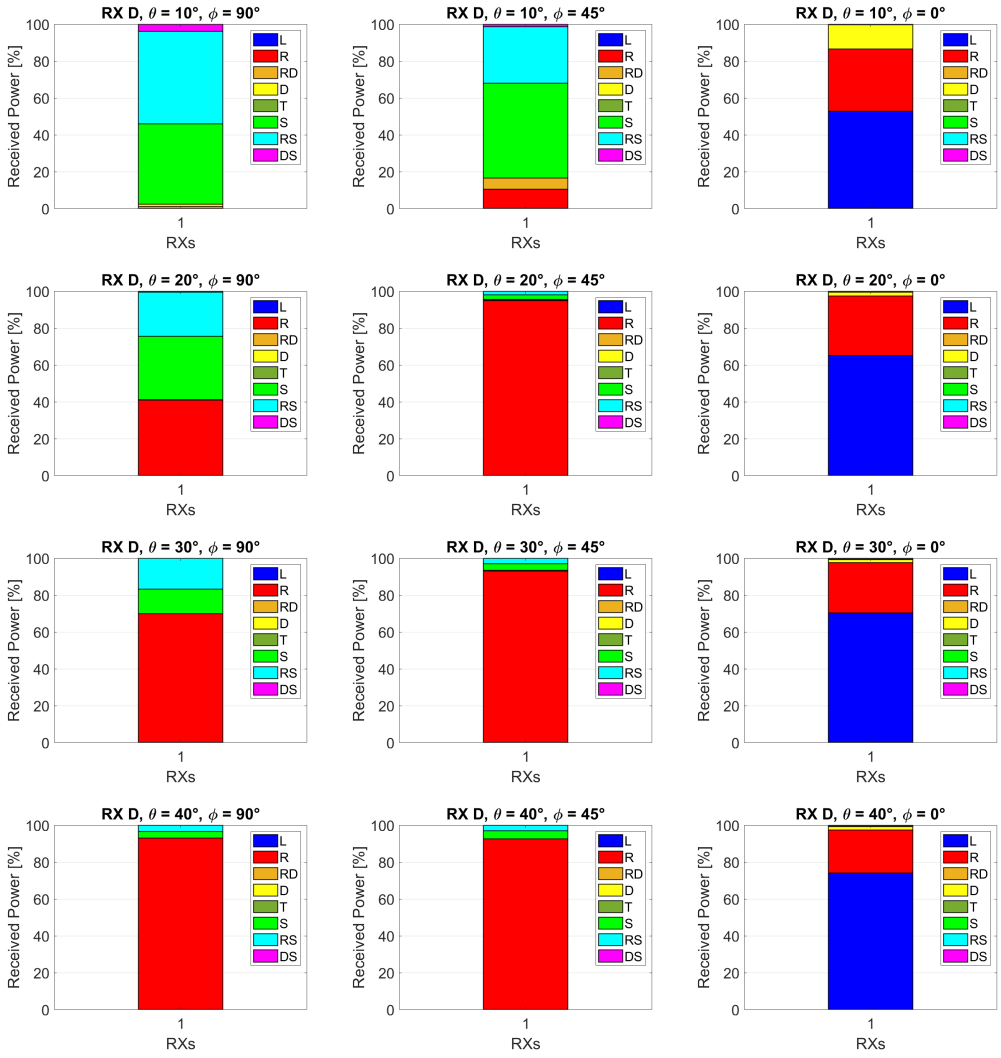

Figure 3.7: Histograms of the percentage of the total received power associated with the rays of each mechanism for the grid in position D, all azimuth angles and elevation from 10° to 40°

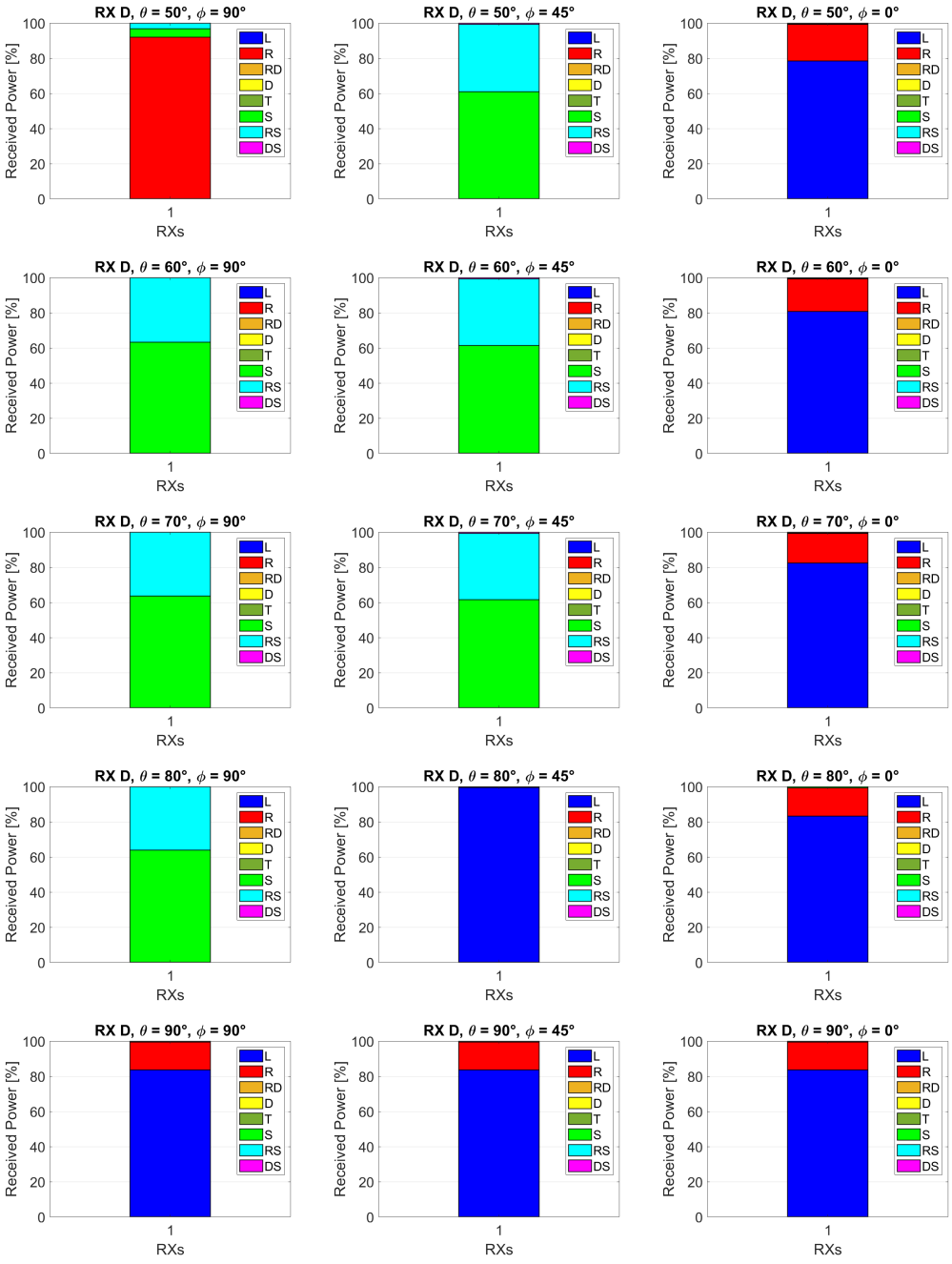

Figure 3.8: Histograms of the percentage of the total received power associated with the rays of each mechanism for the grid in position D, all azimuth angles and elevation from 50° to 90°

Receiver E (Figure 3.9, 3.10)

- Azimuth 90°: almost identical to D;
- Azimuth 45°: at 30° elevation reflections disappear and diffraction and scattering are dominant. Between 80° and 90° LoS and reflection from the floor make their entrance;
- Azimuth 0°: similar to D.

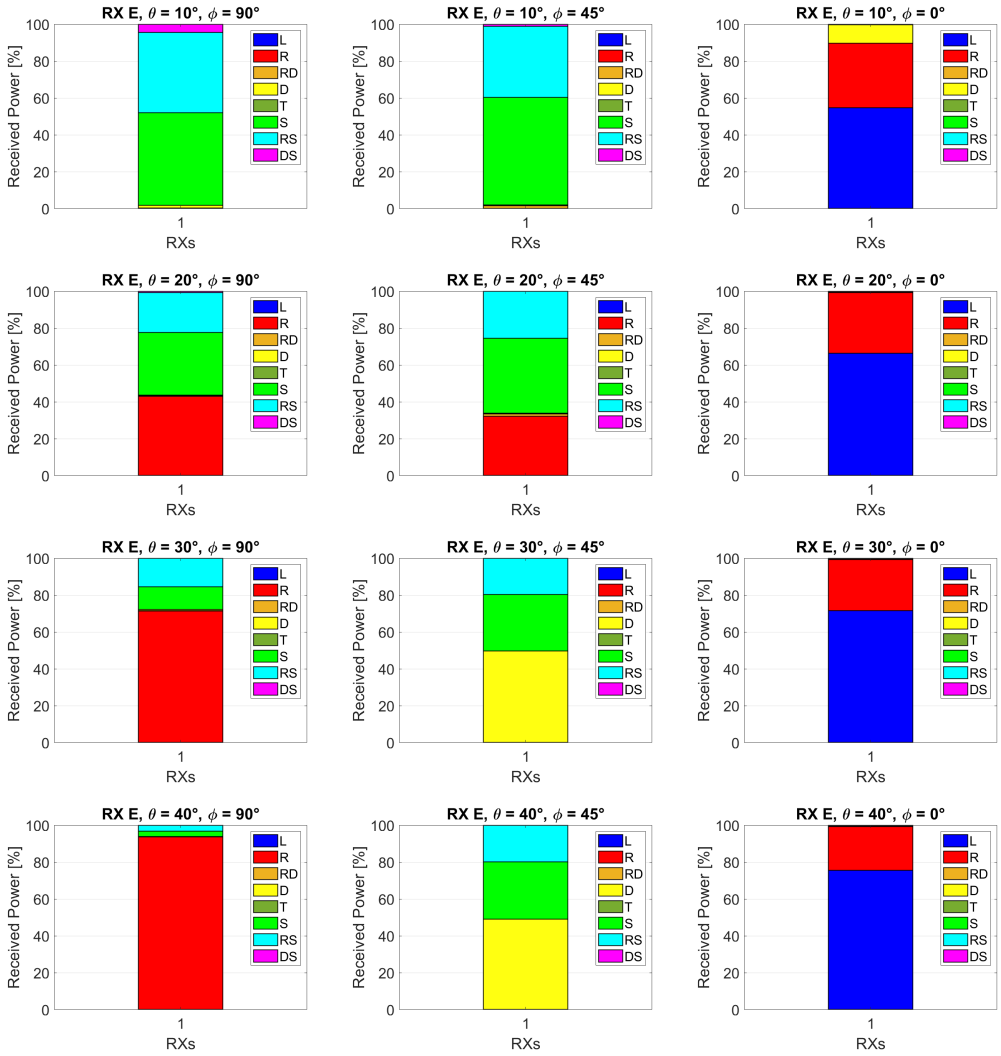

Figure 3.9: Histograms of the percentage of the total received power associated with the rays of each mechanism for the grid in position E, all azimuth angles and elevation from 10° to 40°

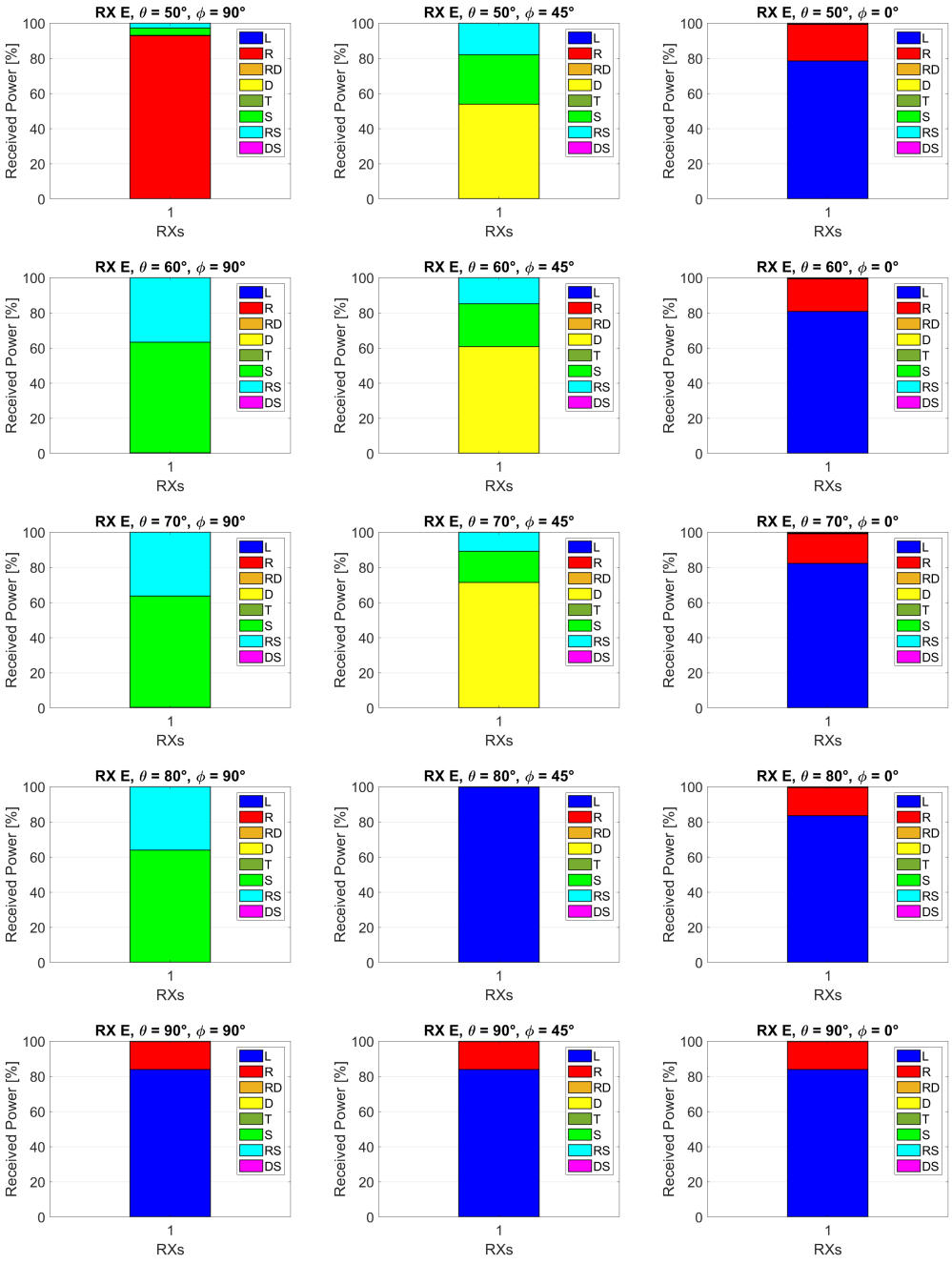

Figure 3.10: Histograms of the percentage of the total received power associated with the rays of each mechanism for the grid in position E, all azimuth angles and elevation from 50° to 90°

Receiver F (Figure 3.11, 3.12)

- Azimuth 90°: LoS dominant, reflection goes from 40 to 20% as elevation increases;
- Azimuth 45°: at 30° reflections take over until LoS becomes dominant at 30°;
- Azimuth 0°: similar to D with the exception that diffraction is less visible at 10° but more visible at 20°.

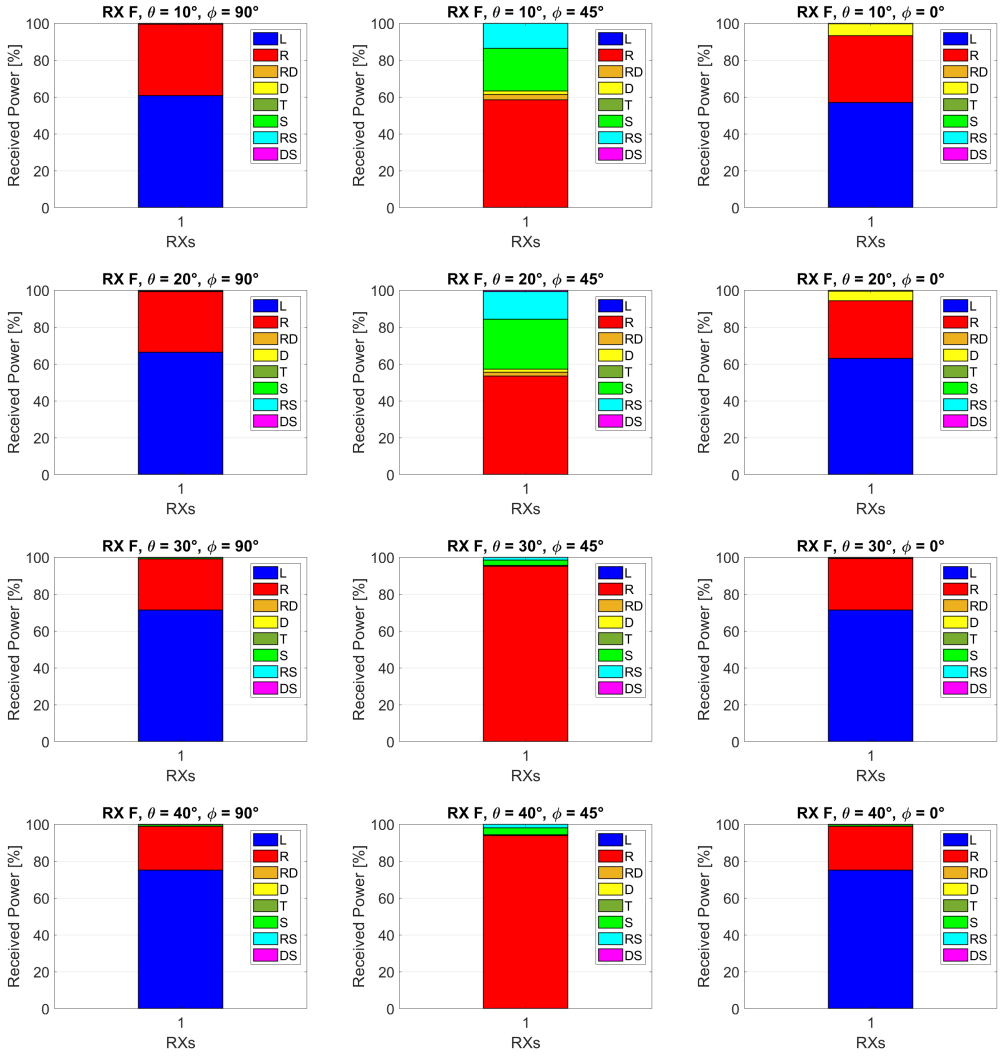

Figure 3.11: Histograms of the percentage of the total received power associated with the rays of each mechanism for the grid in position F, all azimuth angles and elevation from 10° to 40°

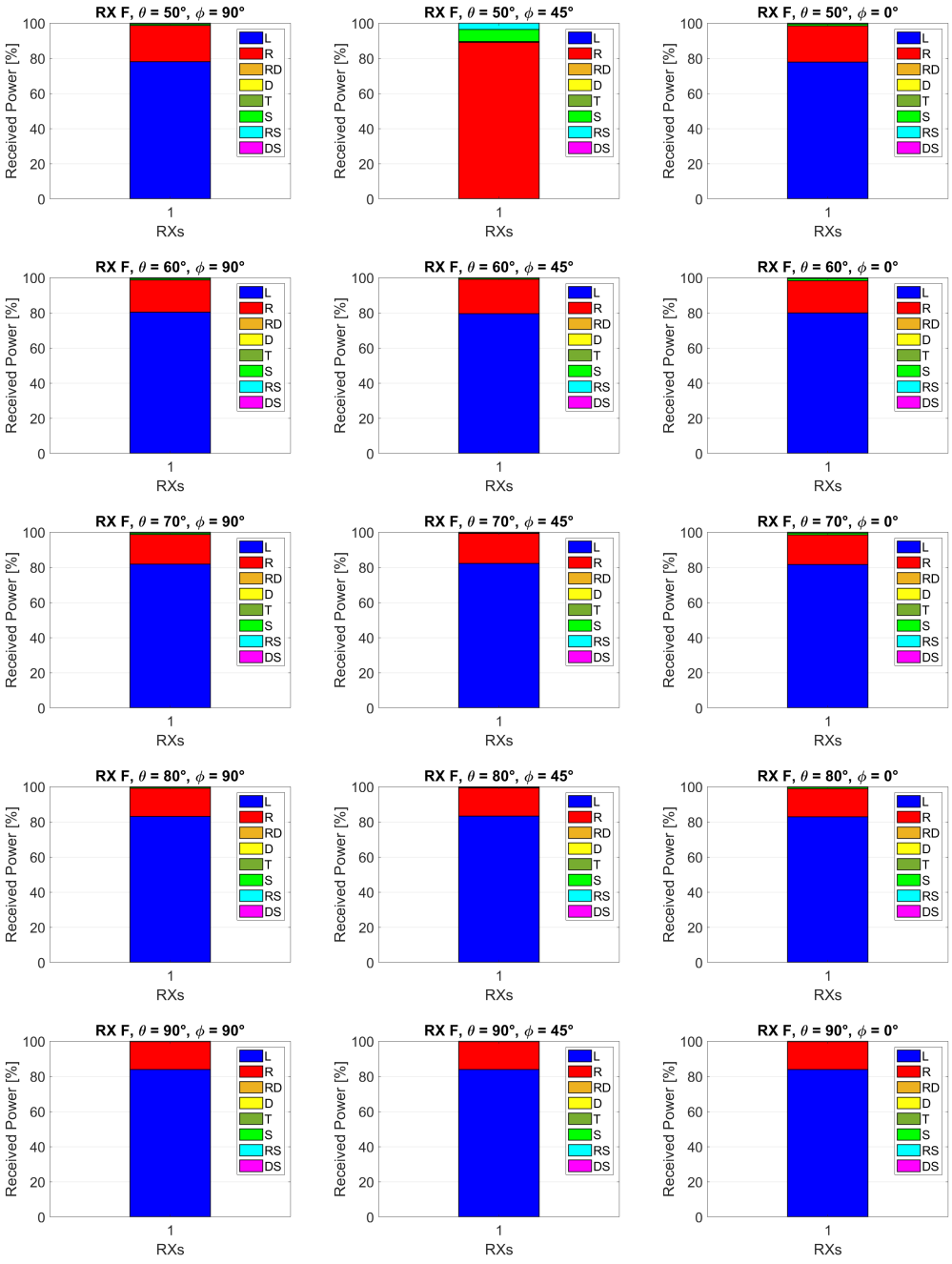

Figure 3.12: Histograms of the percentage of the total received power associated with the rays of each mechanism for the grid in position F, all azimuth angles and elevation from 50° to 90°

Receiver G (Figure 3.13, 3.14)

- Azimuth 90°: perfectly in agreement with the simplified 2D analysis;
- Azimuth 45°: LoS appears earlier than in the case with azimuth 90°, furthermore the diffraction is more present at lower elevations;
- Azimuth 0°: identical to D.

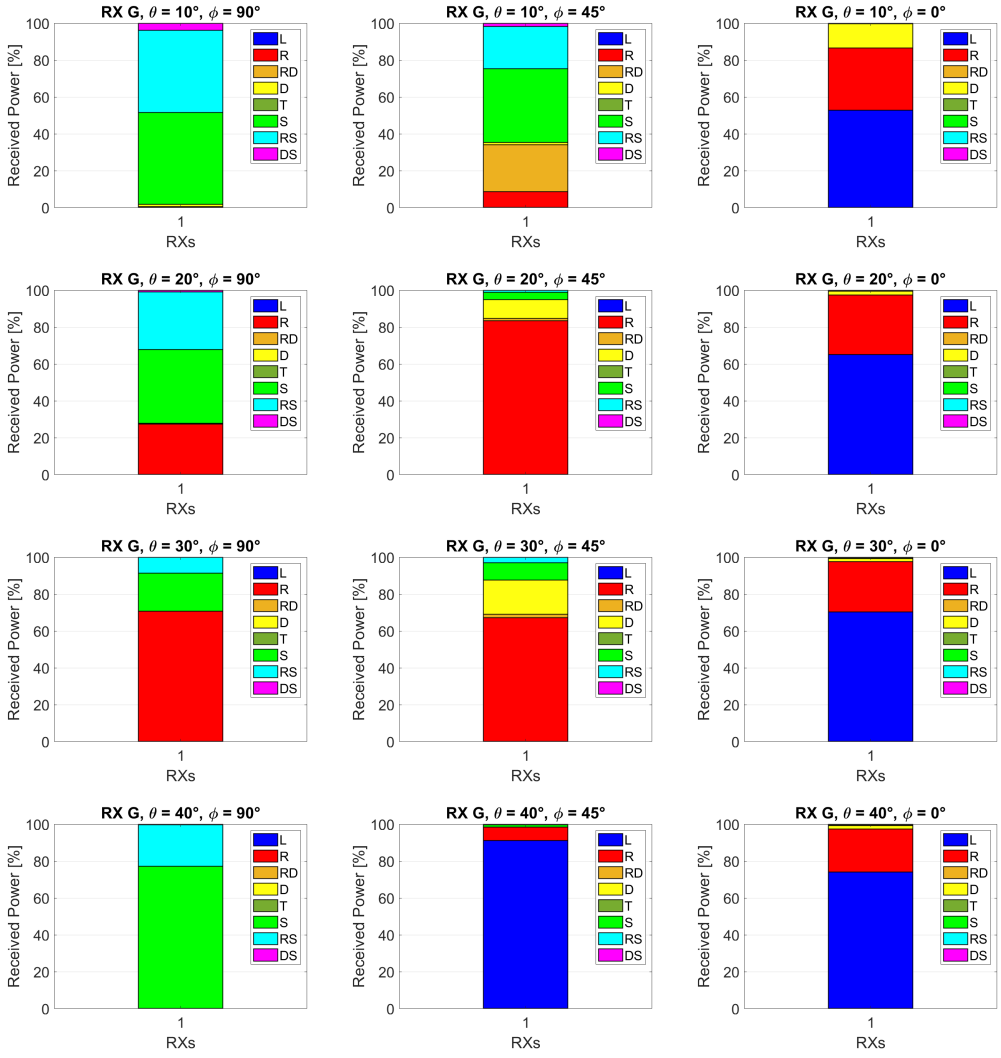

Figure 3.13: Histograms of the percentage of the total received power associated with the rays of each mechanism for the grid in position G, all azimuth angles and elevation from 10° to 40°

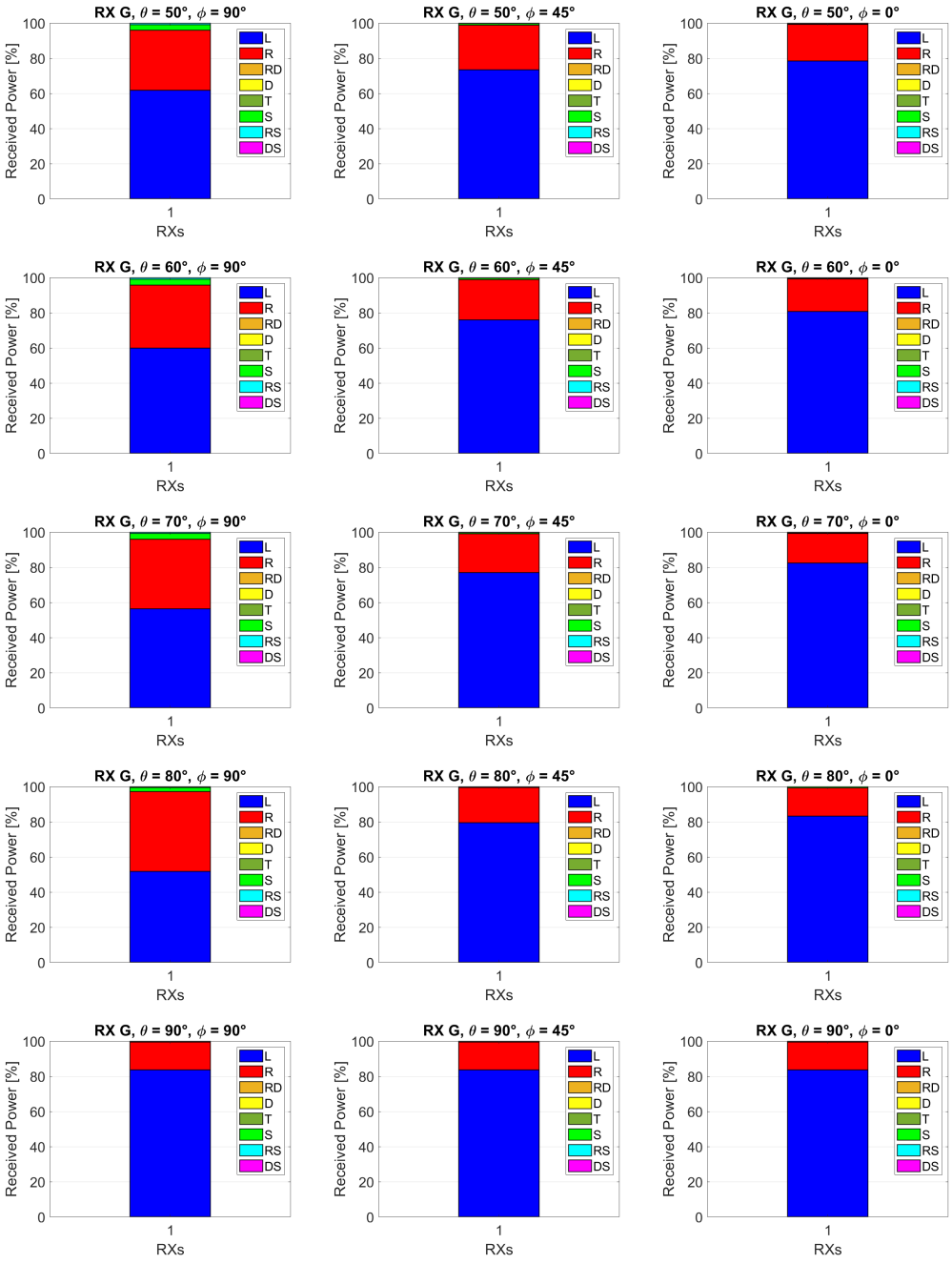

Figure 3.14: Histograms of the percentage of the total received power associated with the rays of each mechanism for the grid in position G, all azimuth angles and elevation from 50° to 90°

Receiver H (Figure 3.15, 3.16)

- Azimuth 90°: very similar to G;
- Azimuth 45°: LoS appears way sooner than in the 90° azimuth case;
- Azimuth 0°: identical to E.

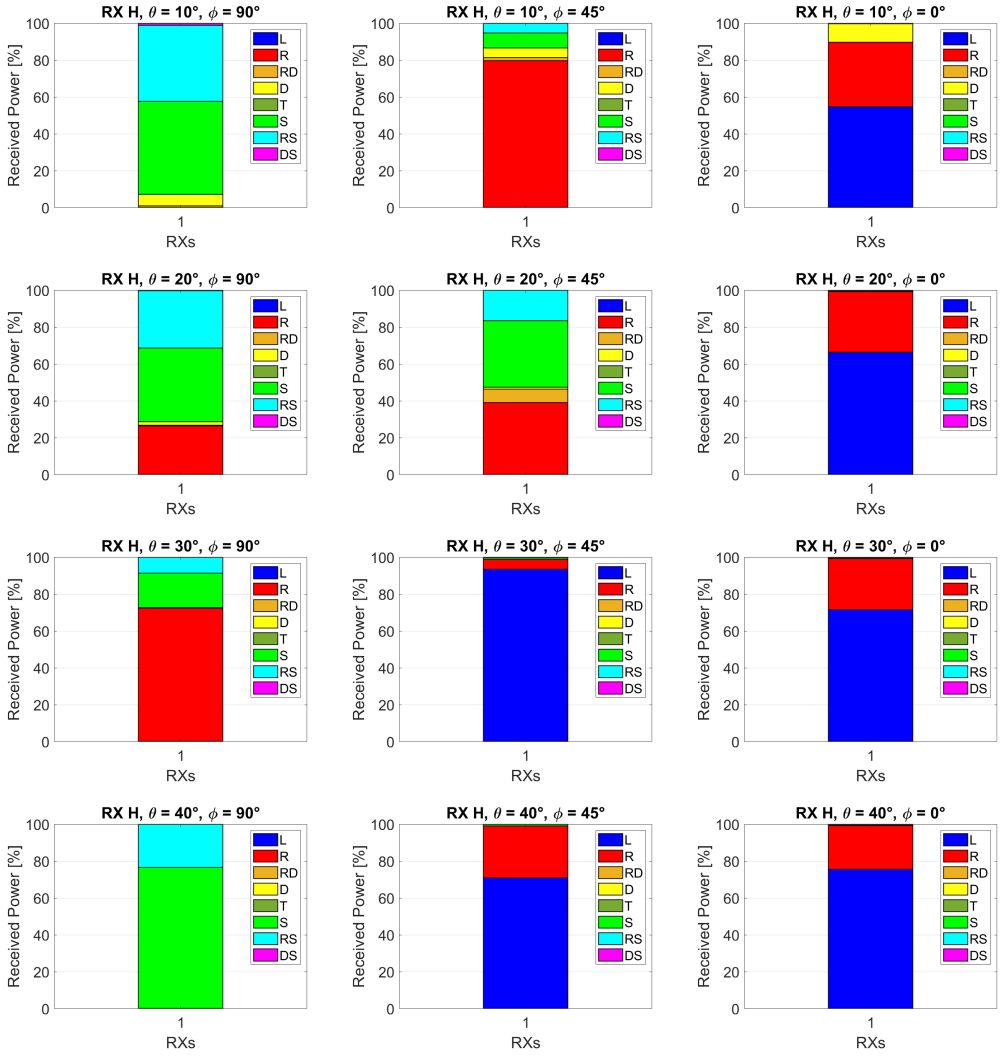

Figure 3.15: Histograms of the percentage of the total received power associated with the rays of each mechanism for the grid in position A, all azimuth angles and elevation from 10° to 40°

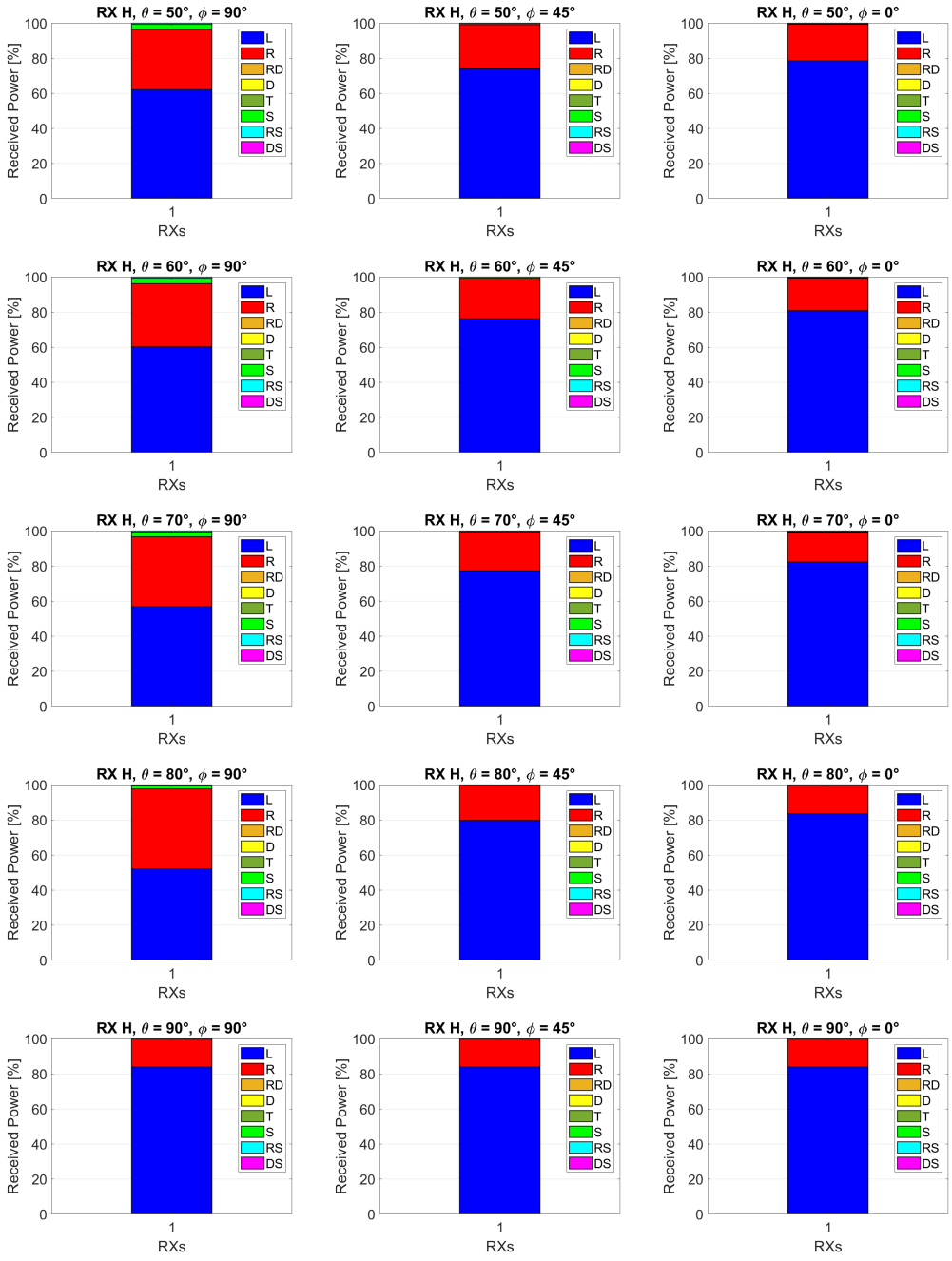

Figure 3.16: Histograms of the percentage of the total received power associated with the rays of each mechanism for the grid in position H, all azimuth angles and elevation from 50° to 90°

Receiver I (Figure 3.17, 3.18)

- Azimuth 90°: LoS dominant, reflection goes from 40 to 20% as elevation increases;
- Azimuth 45°: dominant scattering up to 40° elevation then LoS appears;
- Azimuth 0°: identical to F.

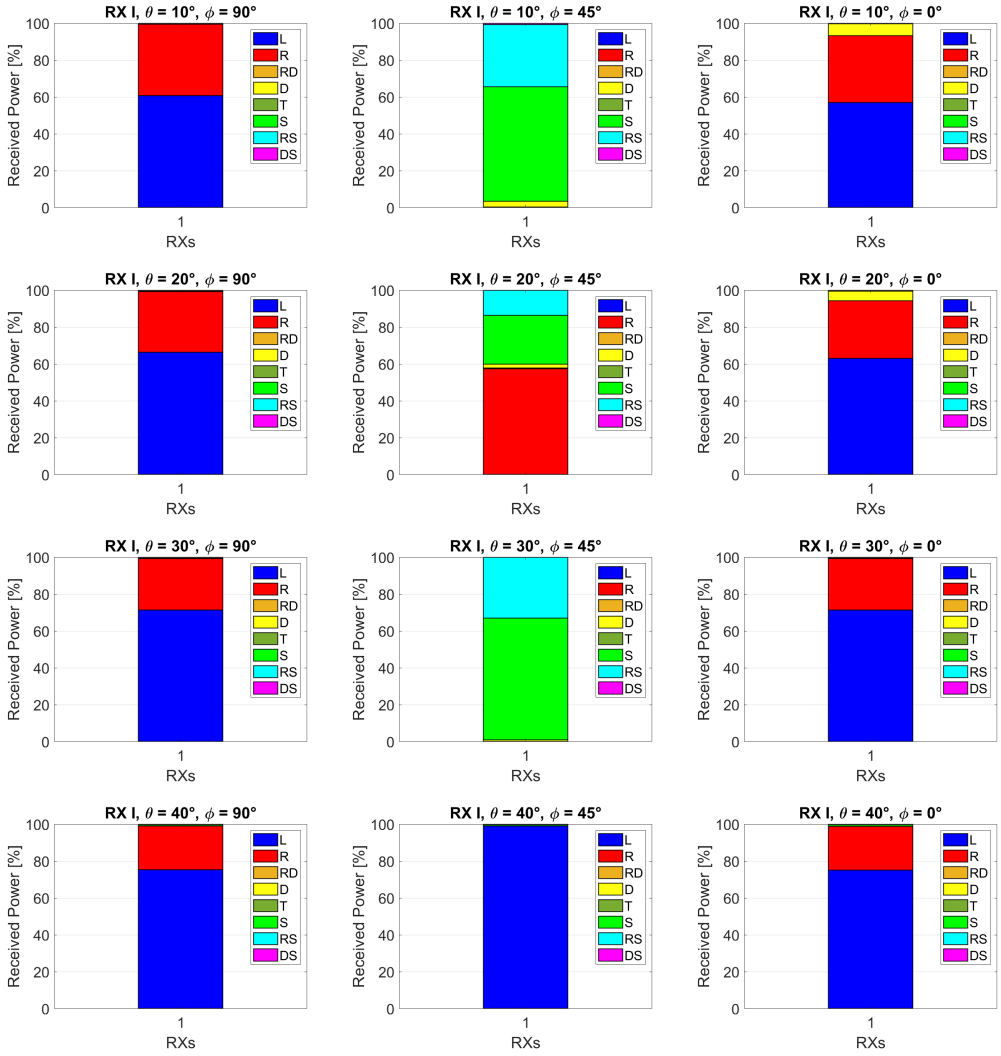

Figure 3.17: Histograms of the percentage of the total received power associated with the rays of each mechanism for the grid in position I, all azimuth angles and elevation from 10° to 40°

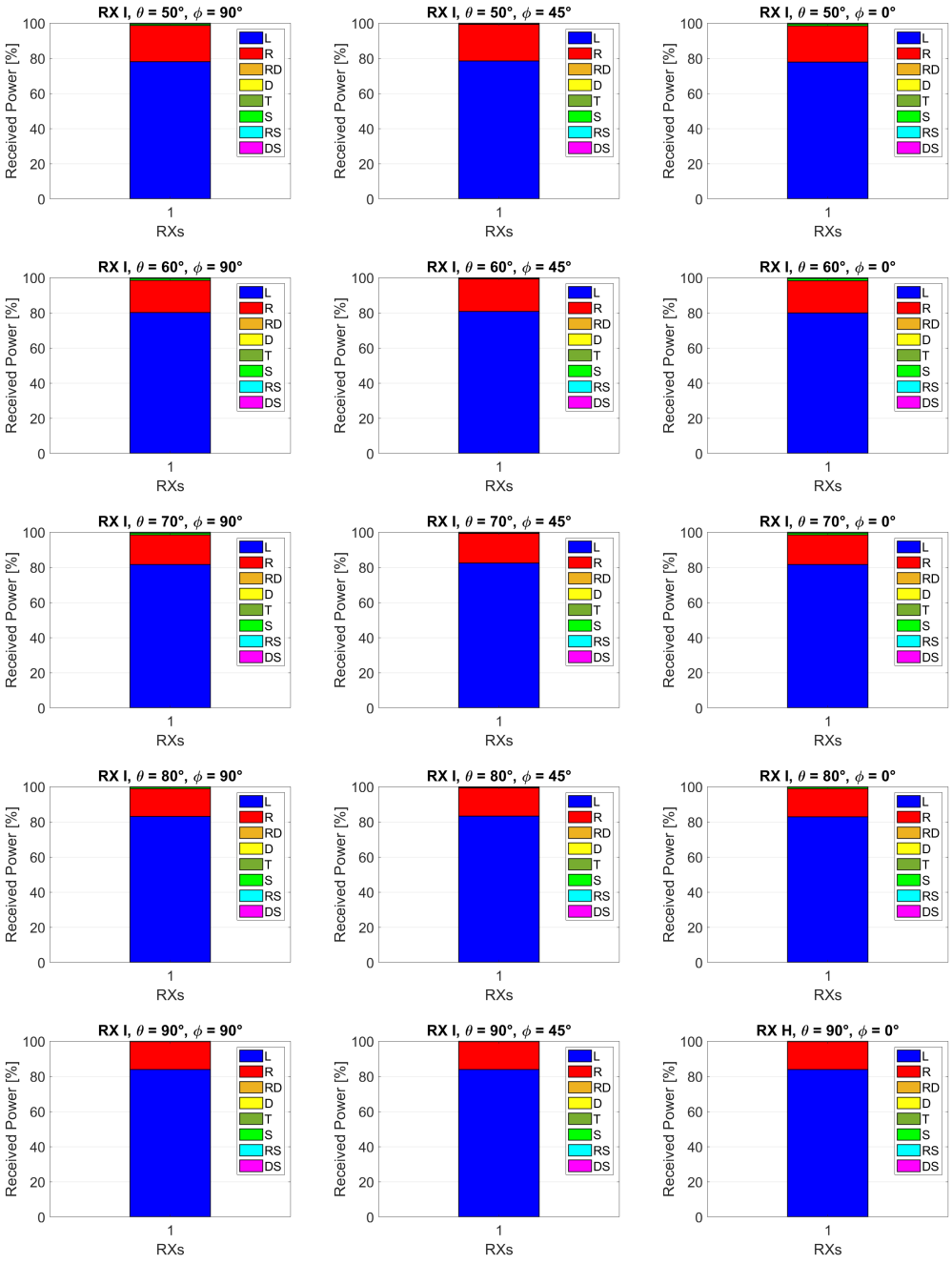

Figure 3.18: Histograms of the percentage of the total received power associated with the rays of each mechanism for the grid in position I, all azimuth angles and elevation from 50° to 90°

To sum up what has been observed, we can say that at azimuth 90° the points that are not in the middle of the intersection follow the 2D approximation very well. At azimuth 45° the alternation of the mechanisms becomes considerably more complicated also favoring, at low/intermediate elevation angle, mechanisms such as scattering and diffraction, the latter was almost not visible at azimuth 90°. At azimuth 0°, as there is always LoS, the only visible mechanisms are often LoS and reflections. It should be noted that at low elevations the combined mechanism of reflection+scattering has an importance comparable to scattering, whereas diffraction+scattering are almost all the time negligible.

3.2 Results of K-factor simulations

The tables containing the previously discussed K-factor tables are shown in section B of the appendix (Tables B.1, B.3, B.5). The K-factor values that we obtained are in the 20 dB / 30 dB range and in some cases can exceed 40 dB The results for 90°, 45°, 0° azimuth angles are analyzed separately:

- **90° azimuth**: the trend of the K-factor is slowly increasing as the elevation angle increases for all receivers except for C, F, I that are located at the center of the intersection. For these 3 points, in fact, the K-factor is higher already from low elevations given that LoS is always present. For the other points, as expected, the K-factor has the maximum value for high elevations, therefore 80° or 90° i.e. when LoS is dominant followed by reflection from the ground. Figure 3.19 represents the sample average value of the K factor in dB as a function of the elevation, also showing the standard deviation of the values. It can be observed that the trend is slowly increasing and that the largest oscillation of the values for the 9 positions of the receivers occurs when the elevation is 10°;

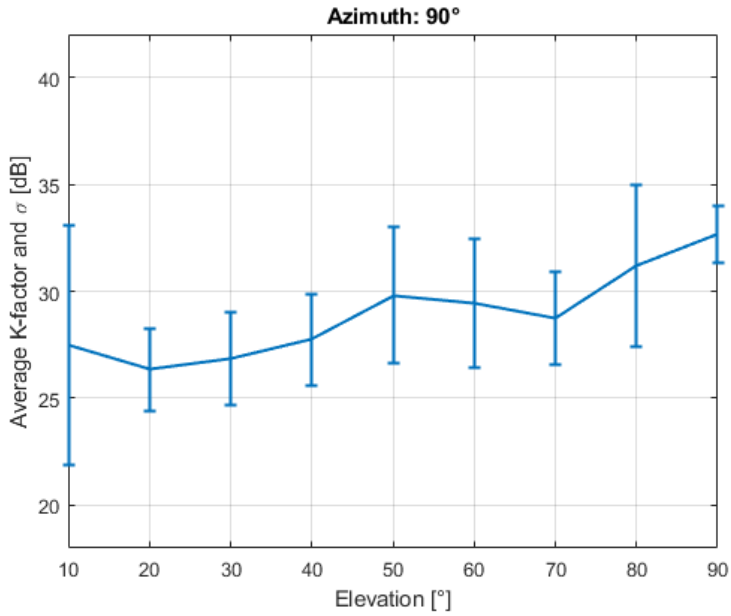

Figure 3.19: Average value of the K-factor in dB and standard deviation on the 9 positions as a function of the elevation and for 90° azimuth

- **45° azimuth**: the trend of the K-factor is clearly increasing with elevation for any receiver since there are no longer some receiver that are always subject to LoS. The average value in dB of the K-factor shows an increasing trend as well except for 90° elevation (Figure 3.20). Now for low elevations the dispersion of values is more contained, while it is maximum at 60°.;

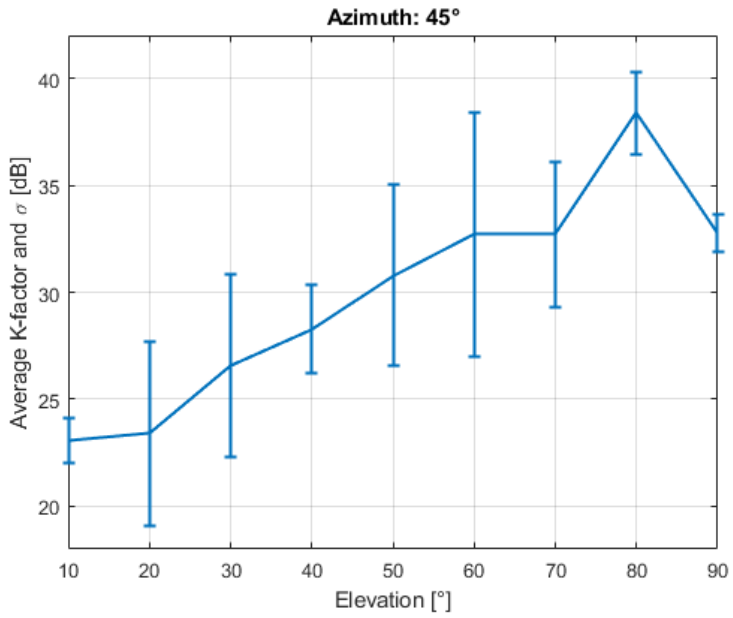

Figure 3.20: Average value of the K-factor in dB and standard deviation on the 9 positions as a function of the elevation and for 45° azimuth

- **0° azimuth**: at 0° azimuth there is always LoS for all receivers, therefore this table is the one that presents the highest values of the K-factor on average. This also means that the trend is not strictly increasing with the elevation increases both in terms of the individual receivers and the average value (Figure 3.21). 10° elevation returns to be the case in which the oscillations of the K-factor values, when moving from one position to another, are stronger.

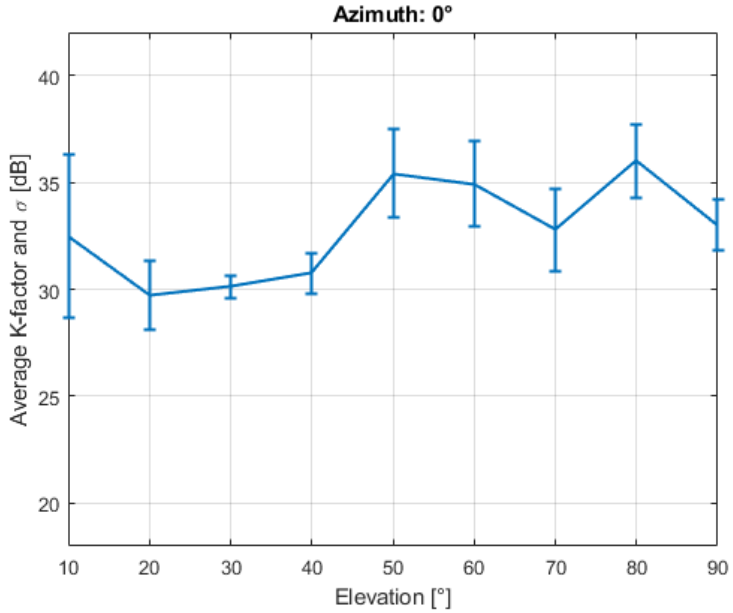

Figure 3.21: Average value of the K-factor in dB and standard deviation on the 9 positions as a function of the elevation and for 0° azimuth

3.2.1 Comparison with 3GPP tables

Comparing the tables with the ones from the 3GPP model in [3] (summarized in Figure 1.1) we observe that the K-factor trend is clearly different. In the 3GPP tables for the S-band urban case the K-factor decreases sharply as the elevation increases, going from 40 dB to 10 dB within 20° of elevation. This trend is completely counter-intuitive and since neither the azimuth angle nor the position of the receiver with respect to the buildings is specified, it is not clear which situation is being referred to. The results of this work are obtained through more realistic simulations and do not lead to any contradictions compared to what was expected.

Conclusions and potential future developments

In conclusion, in this work we initially discussed the importance of NTN in future generation wireless networks and presented the main problems in the current 3GPP NTN model, in particular in the tables of the propagation parameters such as the K-factor. The final aim was to calculate the values of the K-factor in a reference urban environment and for S-band frequencies in order to verify whether the counter-intuitive trends of the K-factor reported in the 3GPP model could also be found in more realistic simulations.

First of all we considered an ideal urban scenario capable of representing a reference for a wide range of environments and analyzed the role of each propagation mechanisms on the total received power in relation to the relative position of transmitter and receiver. Having acquired a good knowledge of the propagation environment we moved on to the statistical characterization of fast fading using 9 grids of receivers placed in reference positions. Modeling the fast fading through the Rice model, we were able to estimate the K-factor for each one of the 9 positions, for several elevation and azimuth angles. The trends of the K-factor as the elevation increases are typically increasing and reflect expectations. The realistic simulations that we carried out confirm that the tables of the K-factor values in the 3GPP model are incorrect as they present completely unrealistic and incomprehensible trends at least as regards the urban environment and the S band studied in this work. This is most likely due to the use of ray-tracing simulations that are not physically consistent and which neglect fundamental mechanisms such as scattering.

The new K-factor tables obtained in this work represent not only a more realistic dataset but also represent a more complete characterization of the environment since they also contemplate azimuthal angle dependence. This could lead to a re-parameterization of the 3GPP NTN channel model for each type of scenario or to the proposal of an entirely new model based on simulation results or propagation theory considerations.

Future continuations of the work:

In the near future this work will most likely be extended and enriched. First of all, it is necessary to consider not only urban scenarios but also dense urban, suburban and rural ones (we can simply change the geometric parameters of the buildings according to table 2.1). Then, the same simulations also remain to be carried out for Ka band frequencies. Furthermore, once the all reference results have been obtained on ideal environments, it will be necessary to simulate some realistic propagation environments (such as the one in Figure 3.22) to verify how the greater complexity in the geometry of the scenario will impact the K-factor. It is expected that, as there is greater multipath richness, the K-factor will tend to be lower.

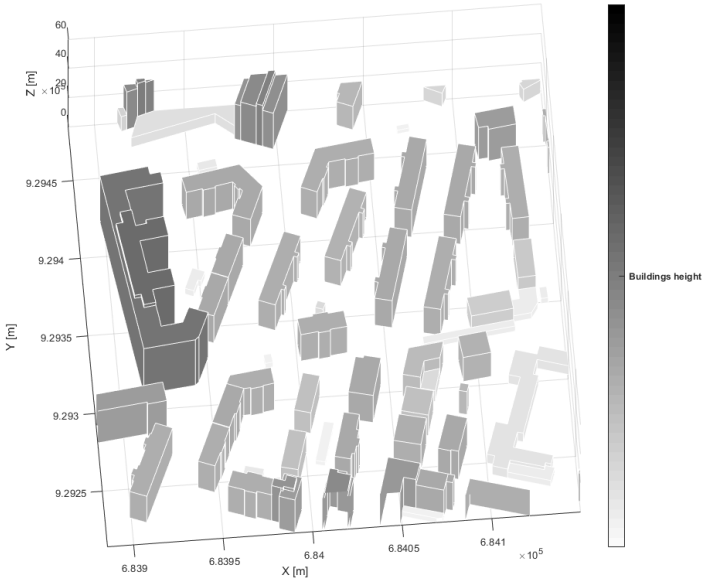

Figure 3.22: Example of a realistic propagation environment: an urban area in the city of Bologna

Lastly, by running the simulations on a workstation with higher computing power, it will be possible to position a much higher number of receiver grids in the environment. This will lead to obtaining a way more precise characterization of how the K-factor values are spatially distributed in a certain area.

Appendix A

Position of the transmitters

The aim of this section is to calculate the position of any possible transmitter $\bar{r}_{TX} = [x_{TX},\, y_{TX},\, z_{TX}]^T$, given:

- The point of reception in which we assume all receivers are condensed $\bar{r}_{RX} = [x_{RX},\, y_{RX},\, z_{RX}]^T$;
- The direction of the street identified by the versor $\hat{d} = [d_x,\, d_y,\, 0]^T$;
- The elevation angle of the transmitter θ.
- The azimuth angle of the transmitter ϕ;
- The desired height of the transmitters when $\theta = 45°$, h_{45};

Some of the input parameters are represented in Figure A.1. Let $\bar{r}_{TX0}$ be vector associated with the position of an hypothetical transmitter having elevation angle θ and azimuth angle equal to 0. We can define the vector $\bar{v} = \bar{r}_{TX0} - \bar{r}_{RX}$ and we can write

$$\bar{v} = \sqrt{2}\ (h_{45} - z_{RX}) \left(\cos\theta\ \hat{d} + \sin\theta\ \hat{i}_z\right)$$

Where $\hat{i}_z = [0,\, 0,\, 1]^T$. Now rotating by ϕ the component of $\bar{v}$ projected onto the xy plane and adding the result to $\bar{r}_{RX}$ we obtain the coordinates of the transmitter:

$$\bar{r}_{TX} = \bar{r}_{RX} + \begin{pmatrix} \cos\phi & -\sin\phi & 0 \\ \sin\phi & \cos\phi & 0 \\ 0 & 0 & 1 \end{pmatrix} \bar{v}$$

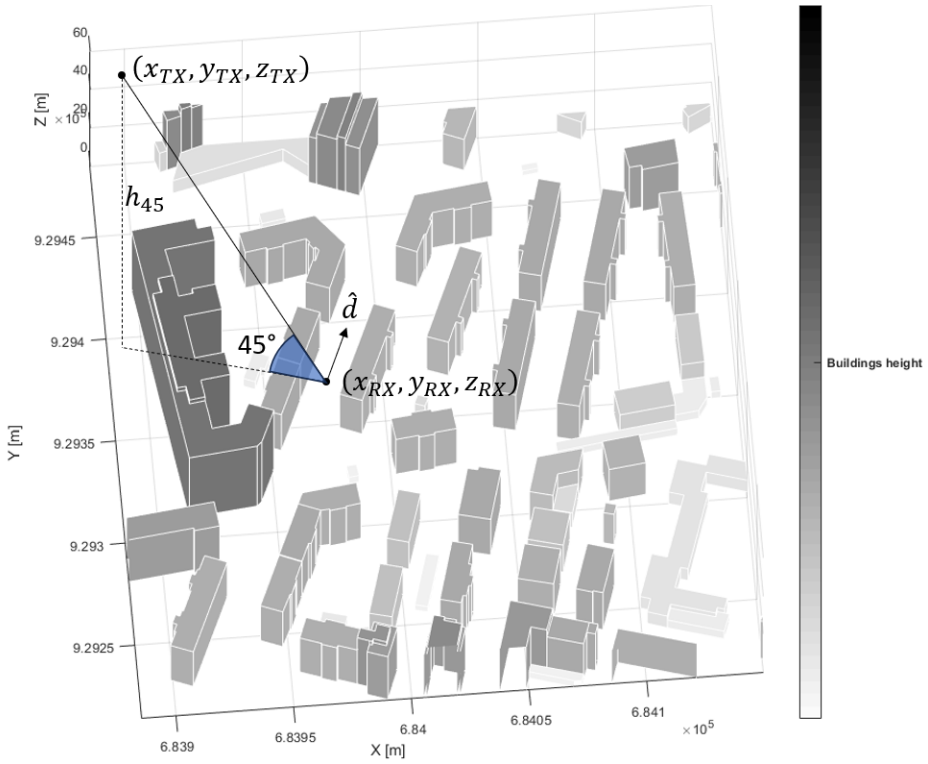

Figure A.1: Vectors and points that are considered when calculating the position of the transmitter in a given environment

Appendix B

K-factor tables

This section contains the K-factor tables to which we refer in section 3.2. We start from the case with 90° azimuth and end with 0° azimuth. The sample mean value and standard deviation (μ and σ) obtained by averaging with respect to the spatial position are also shown. All the K-factor values are in dB.

B.1 Azimuth 90°

RX / θ	A	B	C	D	E	F	G	H	I
10°	24.81	25.19	40.29	24.23	23.67	30.52	23.43	24.09	30.96
20°	25.03	25.78	29.58	24.75	24.14	28.24	24.84	26.54	28.09
30°	25.96	25.69	29.71	24.81	25.02	29.60	25.15	25.95	29.89
40°	26.58	27.60	30.35	28.28	27.03	29.83	24.47	25.18	30.28
50°	26.70	27.54	34.81	27.52	27.40	33.35	28.27	28.94	33.72
60°	26.37	27.78	33.45	26.35	27.12	33.11	28.56	29.01	33.18
70°	28.61	29.20	30.66	25.46	26.74	31.41	27.81	27.26	31.75
80°	32.21	33.08	33.60	24.62	25.18	34.77	30.95	31.54	34.57
90°	31.17	31.93	34.09	31.60	32.67	33.15	31.73	32.26	35.22

Table B.1: K-factor values in dB, for 90° azimuth, as a function of elevation and the position of the grid of receivers

θ / $(*)$	10°	20°	30°	40°	50°	60°	70°	80°	90°
μ [dB]	27.47	26.33	26.86	27.73	29.81	29.44	28.77	31.17	32.65
σ [dB]	5.60	1.90	2.19	2.15	3.20	2.99	2.18	3.78	1.31

Table B.2: Sample mean value and standard deviation of the K-factor (both in dB) for 90° azimuth. (*) = Statistical parameters for the K-factor

B.2 Azimuth 45°

RX / θ	A	B	C	D	E	F	G	H	I
10°	23.12	23.61	24.15	22.41	22.56	24.12	20.82	23.31	23.69
20°	20.91	25.95	26.14	20.23	25.67	26.17	13.82	24.97	26.66
30°	27.80	29.71	26.81	28.56	26.50	16.91	23.83	32.09	26.86
40°	27.67	27.66	27.96	27.65	28.03	24.38	29.88	29.15	32.13
50°	26.65	31.92	27.98	26.79	27.53	28.12	35.20	36.32	36.56
60°	36.43	37.42	36.24	26.85	26.31	22.86	34.07	37.93	36.18
70°	33.98	36.19	33.98	26.61	27.53	33.01	33.16	36.13	33.86
80°	38.39	41.71	36.84	37.11	38.73	36.90	37.05	41.38	37.32
90°	32.10	32.06	33.87	32.44	32.64	34.05	31.81	32.30	33.74

Table B.3: K-factor values in dB, for 45° azimuth, as a function of elevation and the position of the grid of receivers

θ / $(*)$	10°	20°	30°	40°	50°	60°	70°	80°	90°
μ [dB]	23.09	23.39	26.56	28.28	30.79	32.70	32.72	38.38	32.78
σ [dB]	1.05	4.30	4.28	2.08	4.23	5.72	3.40	1.91	0.87

Table B.4: Sample mean value and standard deviation of the K-factor (both in dB) for 45° azimuth. (*) = Statistical parameters for the K-factor

B.3 Azimuth 0°

RX / θ	**A**	**B**	**C**	**D**	**E**	**F**	**G**	**H**	**I**
10°	34.21	34.67	35.93	30.69	36.26	27.01	30.55	36.08	26.87
20°	30.96	31.49	31.26	30.94	29.59	27.16	29.77	28.76	27.66
30°	30.44	30.88	29.97	30.09	30.74	29.33	29.75	30.38	29.56
40°	30.77	31.79	30.01	31.40	31.29	29.53	31.46	31.34	29.14
50°	34.99	37.58	33.40	36.38	37.70	33.09	36.08	37.13	32.33
60°	35.85	37.51	32.83	35.56	36.21	32.64	35.46	36.55	31.70
70°	32.44	34.82	30.95	32.72	34.91	30.26	32.80	35.39	30.61
80°	35.99	37.83	34.36	35.37	37.91	33.82	36.62	38.10	33.98
90°	30.52	32.70	34.59	32.78	33.37	34.17	32.16	32.88	33.78

Table B.5: K-factor values in dB, for 0° azimuth, as a function of elevation and the position of the grid of receivers

θ / (∗)	10°	20°	30°	40°	50°	60°	70°	80°	90°
μ [dB]	32.48	29.73	30.13	30.75	35.41	34.92	32.77	36.00	32.99
σ [dB]	3.80	1.59	0.53	0.96	2.04	2.02	1.94	1.72	1.21

Table B.6: Sample mean value and standard deviation of the K-factor (both in dB) for 0° azimuth. (*) = Statistical parameters for the K-factor

Appendix C

Property of Rice distribution

This section contains the proof of the following property.

Let X be a random variable with Rice distribution: $X \sim \text{Rice}\,(\nu_X, \sigma_X)$. Hence its pdf is

$$f_X(x) = \frac{x}{{\sigma_X}^2} \exp\left(\frac{-\left(x^2 + {\nu_X}^2\right)}{2{\sigma_X}^2}\right) I_0\left(\frac{x\,\nu_X}{{\sigma_X}^2}\right) \tag{C.1}$$

Where $I_0\,()$ is the modified Bessel function of the first kind with order zero. Let Y be another random variable which is function of X, more specifically

$$Y = kX$$

Where k is a positive deterministic constant.

Then the pdf of Y is

$$f_Y\,(y) = \frac{1}{k} f_X\left(\frac{y}{k}\right)$$

Therefore we have $Y \sim \text{Rice}\,(\nu_Y = k\,\nu_X\ ,\ \sigma_Y = k\,\sigma_X)$

Proof:

Let us denote by $F_Z(z)$ the cumulative distribution function (cdf) of a certain random variable Z.

From the definition of Y we can write

$$f_Y(y) = \frac{\mathrm{d}}{\mathrm{d}y} F_Y(y) = \frac{\mathrm{d}}{\mathrm{d}y} \Pr\left(Y \leq y\right) = \frac{\mathrm{d}}{\mathrm{d}y} \Pr\left(kX \leq y\right) =$$
$$= \frac{\mathrm{d}}{\mathrm{d}y} \Pr\left(X \leq \frac{y}{k}\right) = \frac{\mathrm{d}}{\mathrm{d}y} F_X\left(\frac{y}{k}\right) = \frac{1}{k} f_X\left(\frac{y}{k}\right)$$

Substituting C.1 and rearranging the terms we obtain

$$f_Y\left(y\right) = \frac{y}{\left(k\sigma_X\right)^2} \exp\left(\frac{-\left[y^2 + \left(k\nu_X\right)^2\right]}{2\left(k\sigma_X\right)^2}\right) I_0\left(\frac{y\, k\nu_X}{\left(k\sigma_X\right)^2}\right)$$

This proves that $Y \sim \mathrm{Rice}\left(\nu_Y = k\,\nu_X\ ,\ \sigma_Y = k\,\sigma_X\right)$.

Bibliography

[1] M. Giordani and M. Zorzi, "Non-terrestrial networks in the 6G era: Challenges and opportunities," *IEEE Network*, vol. 35, no. 2, pp. 244–251, 2021.

[2] V. Degli-Esposti, F. Fuschini, and D. Guiducci, "A study on roof-to-street propagation," *IEEE ICEAA '03*, September 8-12 2003.

[3] 3GPP, "Study on new radio (NR) to support non-terrestrial networks: TR 38.811 v15. 4.0," 2020.

[4] ——, "Study on channel model for frequencies from 0.5 to 100 GHz: TR 38.901 v17.0.0," 2022.

[5] E. M.Vitucci, N. Cenni, F. Fuschini, and V. Degli-Esposti, "A reciprocal heuristic model for diffuse scattering from walls and surfaces," *IEEE Transactions on Antennas and Propagation*, pp. 1–12, 2023, accepted for publication.

[6] Report ITU-R M.2135, "Guidelines for evaluation of radio interface technologies for IMT-Advanced," 2008.

Acknowledgements

I would like to thank Professor Degli Esposti and Professor Vitucci for their precious advice, patience and time. Their support and knowledge were of essential importance for the development of the thesis. Finally, a special thanks to my family.